An Observational Study of Protostellar Binary IRAS 16293-2422

Mika Suzuki

The Graduate University for Advanced Studies
Nobeyama Radio Observatory, National Astronomical Observatory of Japan,
Minamimaki, Minamisaku, Nagano 384-13, Japan

Contents

Acknowledgments

I would like to express my thanks to Masato Ishiguro for fruitful discussion. Kohichiro Morita are appreciated for exciting discussion and invaluable help in my research . I acknowledge Ryohei Kawabe for his critical comments and his excellent works in making the receiver system for Nobeyama Millimeter Array. Technical staffs in Nobeyama Radio Observatory, particularly Tomio Kanzawa, Hiroyuki Iwashita, Kazuyuki Handa, Toshikazu Takahashi, and Kiyoshi Nakajima provided me with invaluable help for observations at Nobeyama Radio Observatory. Sachiko K. Okumura and Yasuhiro Murata also helped me much in my observations and data reduction. I learned so much from various discussion with many people, including Takenori Nakano, Shouken Miyama, Masuo Tanaka, Tomofumi Umemoto, and Naomi Hirano. Finally, I thank my friend who helped and encouraged me in various aspects throughout this work.

ABSTRACT

Star formation is one of the most fundamental subjects should be addressed in the modern astrophysics. The study of star formation has a long history and has been successful for the case of single stellar collapse. However it is now well established that approximately two-thirds of all solar-type field stars are members of binary or multiple systems (Duquennoy and Mayor 1991). Binary star formation seems to be a natural process. Hence the primary mechanism by which they form should be identified. In order to establish the exact theory of binary star formation observational constraint is necessary. Observations using millimeter-wave Interferometer are one of the effective way to investigate the environments at small scale around protostellar binary systems, which are still embedded in molecular gas and dust. In this thesis we have made aperture synthesis observations of a candidate of protostellar binary system IRAS 16293-2422, which consists of two radio sources A and B at a separation of 840 AU (Wootten 1989) and has two pairs of molecular outflows (Mizuno *et al.* 1990), and tried to get information leading to an implication for binary formation mechanism.

The aperture synthesis observations for IRAS 16293-2422 were carried out using the Nobeyama Millimeter Array (NMA) with the molecular lines of $C^{32}S$ $J = 2 - 1$, $J = 3 - 2$, and $C^{34}S$ $J = 2 - 1$, and with 98 and 147 GHz continuum emissions.

We derived four features of molecular gas: (1) Rotating disk of the molecular gas just centered at source A, whose mass and size are 0.23 $M_\odot$ and
3200 AU $\times$ 1300 AU, respectively, (2) EW elongation of molecular gas associated with source A whose mass is 0.024 $M_\odot$, (3) Compact blue-wing component centered at source A, whose mass is 0.01 $M_\odot$, and (4) Molecular gas closely associated with source B, whose mass is 0.05 $M_\odot$.

From the continuum emission we derived two kind of dust environments: (1) Compact dust disks surrounding each central protostar, whose masses are 0.01 $M_\odot$ and 0.03 $M_\odot$, respectively. (2) Extended dust envelopes of 500 AU scale around each of source A and B, whose masses are 0.3 $M_\odot$ and 0.5 $M_\odot$, respectively.

In summary, the 2000 AU scale molecular envelope is more massive around source A than source B, while the 500 AU scale dust envelope has almost the same mass. The compact

disk around sources A is less massive than that around source B.

These observational evidences imply that the two sources are in the different evolutionary phases. Around source A a molecular envelope still exists to fall onto a center and a central compact disk have not yet grown. Around source B the envelope begins to disappear, while the accretion disk have grown to possess a large mass. It is very probable that source A is just in an active phase of protostar deeply embedded in the dense gas envelope, considering that source A has free-free emission, H_2O masers, and shocked molecular gas (Wootten 1989; Mundy *et al.* 1992). Source B might be in elder protostar phase than source A or in young T Tauri phase. An age difference between sources A and B is estimated to be 10^4 - 10^6 years.

We investigate the kinematics and dynamical instability of the molecular gas disk around source A. The rotation velocity seems to be roughly consistent with or slightly smaller than estimated Keplerian velocity. However it is not clear whether the disk is rotationally supported or not, because of large uncertainties in the rotation velocity and the stellar mass. The disk mass of 0.53 $M_\odot$ (the compact dust envelope and the gas disk) is comparable to or higher than the stellar mass of 0.2- 0.5 $M_\odot$. This means that the disk is actually unstable.

The configuration of the binary system is estimated using the quantities obtained by our observations. The estimated configuration implies that the plane of the binary orbit and that of the disk around source A is not coplanar. Hence it is possible that the gas disk around source A may precess around the binary axis under the gravitational effect of source B. The disk precession could explain the two outflows originated from source A, which show activities related to the outflows. However, if inner portion of the disk controls the direction of the outflow, it is difficult to explain the multiple outflows by the disk precession.

1 Introduction

Star formation is one of the most fundamental subjects should be addressed in the modern astrophysics. It is believed that stars form in dense molecular gas clouds. Since most line emission of molecular species such as CO, CS, and so on, appear in the radio frequency regime, the progress in the research of star formation strongly depends on that in observational technology of the radio telescope facilities. Since the first detection of molecular line emissions from molecular clouds in our Galaxy (Wilson *et al.* 1970), many great progresses have been made for these 25 years.

The study of global distribution of molecular gases in our Galaxy was conducted by several researchers with use of CO $J = 1 - 0$ emission (*e.g.*, Solomon *et al.* 1979), revealing that there are many giant molecular clouds (GMCs) in our Galaxy disk. These GMCs have been studied extensively and are now considered to be actually cloud complexes, composed of clumps with masses $\sim 10^3$ - 10^4 $M_\odot$, size $\sim$ 2 - 5 pc, and densities $n_{\rm H_2} \sim 10^{2.5}$ cm^{-3} (Sargent 1977; Blitz 1978). These clumps show similar physical properties with the nearby dark clouds like Taurus and ρ Ophiuchi molecular clouds. Such clumps have small and dense cloud cores. Myers and his co-workers (Myers, Linke and Benson 1983, Myers and Benson 1983) have systematically studied the nature of the dense cores in molecular clouds. Their observations have shown that the cores on average have masses of $\sim$ 4 $M_\odot$ and sizes of $\sim$ 0.1 pc. Myers and Benson (1983) suggested that the cores are the site of low-mass star formation. This picture was supported by their close association with known T Tauri stars later (Myers 1986), with bipolar outflow sources (Fuller and Myers 1987), and with IRAS-detected infrared sources in approximately half of the core (Beichman *et al.* 1986). The central sources embedded in cloud cores can be identified as young stellar objects (YSOs) by the characteristics of their infrared spectral energy distributions (SEDs) (Adams and Shu 1986; Adams *et al.* 1987).

It is currently well established that forming stars are deeply embedded in cloud cores, consisting of cold molecular gas and dust. The dust absorbs and/or scatters the light from newly formed stars and re-emits at infrared wavelengths as thermal emission. Since the circumstellar

dust exhibits a wide range of temperatures, the emission have a spectral distribution wider than that of a single temperature blackbody. The shape of the broad band infrared spectrum of YSOs depends both on the nature and distribution of the surrounding dust. Thus the shape of SED is a function of the state of evolution of YSOs (Lada and Wilking 1984; Lada 1991). The currently accepted classification scheme uses the spectral index $\alpha = -dlog\nu F_\nu / dlog\nu$ which is evaluated longward of 2,2 μm to distinguish between three classes: (1) Class I sources have SEDs broader than a single temperature blackbody and for which α is positive, (2) Class II sources have SEDs broader than a single temperature blackbody and for which α is negative, and (3) Class III sources have SEDs close to that of a single temperature blackbody and for which α is negative. These are illustrated in Figure 1.1. Class I sources derive their positive spectral indices from the presence of large amounts of circumstellar dust. These sources are usually deeply embedded in molecular cores and rarely exhibit detectable emission in the optical wavelength. Thus Class I sources have been interpreted as being protostars. Class II sources are usually found to be T Tauri stars or FU Ori stars. Their negative spectral indices indicate that class II sources are surrounded by considerably less circumstellar dust than class I sources, probably because most of the original star-forming gas and dust have already been incorporated into the young star. Class III sources are usually optically visible with no or very little excess emission at near- and mid-infrared wavelengths, and therefore no or little circumstellar dust. Class III sources include both young main sequence stars and weak-line T Tauri stars.

The SEDs of class I sources are successfully modeled using a recent physically self-consistent theory of protostars developed by Shu and his collaborators. Shu (1977) showed that the collapse of the cloud core, assumed to have density distributions similar to that of an isothermal sphere (i.e., $\rho(r) \propto r^{-2}$), proceeds in an inside-out manner with a flattening of the density gradient within the infalling region (i.e., $\rho(r) \propto r^{-1.5}$). The central protostellar core becomes increasingly luminous as it radiates away the gravitational potential energy lost by the infalling gas. By introducing a slight amount of rotation, Terebey, Shu, and Cassen (1984) showed that collapsing isothermal spheres could, as a consequence of conservation of angular momentum, produce infalling density distributions with central cavities and flattened

central disk-like structure. Using the density distributions derived from such models and taking into account the luminosity radiated by the central disks as well as the protostellar core, Adams and Shu (1986) and Adams, Lada, and Shu (1987) were able to successfully model the observed spectra of numerous class I sources.

The evolutionary sequence of singly formed stars seems to be clear as described above. However some problems remain unsolved: (1) Protostars derive a significant portion of their luminosity from accretion, and in general they should be more luminous than similar mass class II or III sources. Analysis of the luminosity function of the YSOs in the embedded cluster in the ρ Ophiuchi molecular cloud indicated that class I sources were systematically more luminous than class II sources (Wilking, Lada and Young 1989). However this is an indirect evidence of accretion. Where is direct evidence of cloud collapse ? (2) It has long been recognized that many stars are not single stars, but occur rather as members of binary systems (Abt 1983). What happens in the case of binary or multiple star formation ?

1.1 Class 0 sources as protostars surrounded by infalling envelopes

By definition, protostars are objects which derive most of their luminosity from the release of the gravitational potential energy of infalling matter. Although direct observation of the infall onto low-mass protostars remains elusive, we can still identify low-mass protostars via the amount of material present in their circumstellar infall envelopes.

Since 1986 a number of embedded sources have been discovered which display extremely steep infrared energy distributions, referred to as class 0 sources (Andre *et al.* 1994). The spectra of class 0 sources are that of a single blackbody (see Figure 1.1). Numerical calculations of protostellar collapse suggest that the continuum spectra of the youngest protostars should closely resemble that of a blackbody at 10 - 30 K. The youngest protostars are thus so highly obscured by their own circumstellar material that they are undetectable at near-IR and optical wavelengths. Hence the class 0 sources are the youngest stellar objects, probably true protostars at the beginning of the main accretion phase. All class 0 sources are the apparent driving sources of spectacular, well collimated outflows and are associated with VLA

radio continuum emissions. These are consistent with the outflow phase starting as soon as a protostellar core forms at the center of a collapsing cloud core. Inflow and outflow therefore will occur simultaneously (*e.g.*, Lada and Shu 1990). Thus radio continuum emission probably traces free-free radiation from shock-ionized material in the associated wind and/or the accretion shock at the surface of the central object. The class 0 sources known to date are: IRAS 16293-2422, VLA1623, B335, L1448-C, l1448-N, NGC1333 IRS4A/4B, NGC2264G, and L1527 (Barsony 1995).

Recently collapsing or infalling motions are reported to exist for two class 0 sources: IRAS 16293-2422 and B335. Zhou (1995) studied the line formation in collapsing dense cores with rotation in the semianalytic model of Terebey, Shu, and Cassen (1984) (TSC model), and successfully applied the model to IRAS 16293-2422 and B335. IRAS 16293-2422 is a young stellar object at a distance of 160 pc, located in the ρ Ophiuchi molecular cloud. Walker *et al.* (1986) first suggested that its circumstellar gas is collapsing based on the profiles of the $J = 5-4$ and $2-1$ lines of CS and $C^{34}S$. Using a microturbulence model of radiative transfer, they were able to reproduce the line profiles toward the center position of IRAS 16293-2422. Zhou (1995) calculated the distribution of line profile across the surface of the cloud core, and found a best-fit model with the following parameters: the sound speed = 0.5 km s^{-1} , the rotational rate = 3×10^{-13} s^{-1}. B335 is an isolated Bok globule at a distance of 250 pc. Zhou (1995) also found a best-fit model. He argued that the agreement of the observed line profiles of IRAS 16293-2422 and B335 with the TSC model is remarkable and the evidence for infall is very strong for these sources.

1.2 Binary and multiple star formation

The majority of stars in the Galaxy are found in binary or multiple systems and investigation of binary frequency among main sequence field stars has a long history (Batten 1973, Abt 1983, Duquennoy and Mayor 1991). In contrast, the first extensive surveys for multiple systems among pre-main sequence (PMS) stars have been only recently started. A measure of the binary frequency in the Taurus-Auriga association has been gained from several infrared high-

angular resolution surveys: 2.2 μm speckle and InSb-array observations (Leinert *et al.* 1993), the higher resolution speckle survey (Ghez *et al.* 1993), the lunar occultation observations (Simon *et al.* 1992, Richichi *et al.* 1994), and spectroscopic studies (Mundt *et al.* 1983, Mathieu *et al.* 1989). Richichi *et al.* (1994) estimated the frequency of multiple systems to be 60 ±9% between separations of 0.013″to 13″, or 1.8 AU to 1800 AU. Multiple systems clearly comprise a large fraction of the PMS population in the Tau-Aur association. Indeed, these surveys yield PMS binary frequencies roughly twice as high as that found for field MS solar-type binaries in the same range of separations. Ghez *et al.* (1993), who used 2.2 μm speckle observations to search for binaries among 69 young stars in both the Tau-Aur and the Scorpius-Ophiuchus star-forming regions, found a frequency of 60 ±17% for binaries with projected separations between 16 AU and 252 AU. They concluded that the PMS binary frequency is four times higher than that among MS solar-type stars. In addition, they find no significant difference between the Tau-Aur and Sco-Oph star-forming regions in the binary frequencies.

Despite the apparent ubiquity of binaries, astronomers have yet to identify the primary mechanism by which they form. Possible formation mechanisms include: (1). prompt fragmentation of the cloud, *e.g.*, through clouds collisions, after which the fragments collapse to form stars (Chapman *et al.* 1992; Clarke and Pringle 1991), (2). fragmentation during cloud collapse (*e.g.*. Boss 1993), and (3). fragmentation of disks composed of infalling material (Adams *et al.* 1989). However the detailed theoretical studies have just begun.

Evidently, binary star formation can occur prior to the PMS phase of evolution. With the PMS binaries now being open to observational study, the forefront of statistical study will soon move to younger, embedded protostellar binary systems. The discovery rate of candidate protostellar binaries is gradually increasing, including IRAS 16293-2422 (Wootten 1989), NGC1333 IRS4 (Sandel *et al.* 1991), IRAS 19156+1906 in L723 (Anglada *et al.* 1991), and perhaps ρ Oph B1 (Sasselov and Rucinski 1990). IRAS 16293-2422 is at present the most extensively studied candidate protostellar binary. Therefore this is the best source for our high-resolution millimeter-wave observations as the first step of the observational study of binary formation and evolution.

1.3 Introduction to IRAS 16293-2422

IRAS 16293-2422 is located in the eastern streamer region of the ρ Ophiuchi molecular cloud complex at a distance of 160 pc. The bolometric luminosity amounts to $27L_{\odot}$ and its peak appears at far infrared (FIR). The FIR-millimeter spectral energy distribution (Figure 1.2 (a)) is well approximated by a transparent thermal emission of dust at a temperature $\approx$ 40 K with an emissivity law $\kappa_{\nu} \sim \nu^{1.5}$ (Mundy *et al.* 1986, Wootten 1989). This property led Andre *et al.* (1993) to classify it as a Class 0 source which is considered to be an extremely young protostar compared with any classes introduced by Lada (1987). It is remarkable that this object has two pairs of molecular outflows (Walker *et al.* 1988; Mizuno *et al.* 1990, see Figure 1.3 (a)). The spatial extent of the four lobes is $\sim 4'$, which corresponds to $\sim$ 0.2 pc at the distance of 160 pc. Brighter outflow is oriented to east and west, and the other to northeast and southwest. However in the vicinity of IRAS 16293-2422 only east-west bipolar flow is seen (Figure 1.3 (b)). It is also known that IRAS 16293-2422 consists of two discrete centimeter continuum sources whose projected separation is about $5''$, which is 840 AU at a distance of 160 pc (Wootten 1989;, see Figure 1.2 (b)). This fact suggests that IRAS 16293-2422 is a protostellar binary system. Hereafter the SE and NW sources are referred as sources A and B, respectively (Wootten 1989). Recently millimeter continuum mapping also resolved the source into two sources (Mundy *et al.* 1992; Walker *et al.* 1993, see Figure 1.4 (c) and (e)). This assures the presence of two sites of warm dust and strengthens the picture of two protostars in a protobinary system.

The centimeter continuum observations indicate the following difference between the two sources. The spectral index of source A is 0.4 - 0.6, corresponding to typical values of ionized stellar wind or warm shocked region at the interface of a neutral stellar wind and ambient material. On the other hand, that of source B is 1.5 - 2.1, which may be attributed to thermal dust emission (Wootten 1989). Furthermore a cluster of water masers (Wootten 1989, see Figure 1.2 (b)) and SO emission (Mundy *et al.* 1992, see Figure 1.4 (d)) are associated only with source A, indicative of high activity around source A. These differences suggest that the two sources are in different evolutionary phases.

The $C^{32}S$ $J = 2 - 1$, $J = 3 - 2$ and $C^{34}S$ $J = 2 - 1$ emissions have been observed using single dish telescopes (Walker 1986; Menten 1987; Mizuno 1990). The CS molecule has a large dipole moment, so the critical density required to collisionally excite the CS molecule to upper levels is quite high, *i.e.*, $5.7 \times 10^5 cm^{-3}$ for CS $J = 2 - 1$ and $1.5 \times 10^6 cm^{-3}$ for CS $J = 3 - 2$. But detectable lines in both transitions can arise from gas at somewhat lower densities owing to radiative trapping effect. Therefore emission from CS molecule is an useful probe of the denser regions of molecular clouds and in particular around the protostars. The $C^{34}S$ molecule is a modestly abundant isotope of the $C^{32}S$ molecule. The terrestrial sulfur isotopic ratio, $^{32}S/^{34}S$, is 22.5 (Fink 1981), and the observations of molecular clouds (Freaking *et al.* 1980; Schloerb *et al.*1983) indicate that the isotopic ratio in clouds is probably within a factor of 2 of the terrestrial value. Since the excitation requirements for $C^{32}S$ and $C^{34}S$ are almost identical, the only significant differences in their emissions are expected to arise from a large difference in the optical depths of the two species. The optically thin $C^{34}S$ emission will sample the entire column of gas.

The $C^{32}S$ $J = 2 - 1$, $J = 3 - 2$ and $C^{34}S$ $J = 2 - 1$ line profiles taken with the single dish telescopes shown in Figure 1.5 (b) indicate that self-absorption by foreground lower excitation material is probably occurring. The fact that the $C^{34}S$ $J = 3 - 2$ line is singly peaked rules out the possibility that the $C^{32}S$ profiles are due to two velocity components. The narrow component seen in NH_3 and $C^{18}O$ agrees in velocity and linewidth with the absorption seen in $C^{32}S$ $J = 2 - 1$ and $J = 3 - 2$, and so is responsible for the strong self-absorption against the core with much wider CS emission. The $C^{32}S$ $J = 3 - 2$ emission core of size $30'' \times 35''$, which corresponds to 4800×5600 AU at the distance of 160 pc, shows a north-south velocity shift across IRAS 16293-2422 (Figure 1.5 (a)) . This velocity structure is interpreted as a Keplerian-like rotation with a heavily concentrated mass distribution, from model fits including the self-gravity of the gas (Menten 1987). Interferometer map of the $C^{32}S$ $J = 2 - 1$ emission also shows the north-south velocity shift across IRAS 16293-2422 (Walker *et al.* 1993, see Figure 1.4 (a) and (b)), and it is interpreted as a slowly rotating circumbinary disk is present. However the spatial resolution of the earlier observations were so poor to make clear where is the center of the rotating motion. Hence we have undertaken

higher resolution observations of $C^{32}S$ $J = 2-1$, $C^{32}S$ $J = 3-2$ and $C^{34}S$ $J = 2-1$ emissions to study the spatial and velocity structure in the vicinity of IRAS 16293-2422.

Millimeter continuum maps at 98 and 147 GHz are also used to discuss the spatial distribution of dust component. The continuum emission is optically thin and will be a good tracer of the column density of the dust. Furthermore spectral index of the continuum emission is useful tool to investigate the nature of dust component.

1.4 Contents of this thesis

The accumulation of information for protostellar binary systems will expedite the progress of the theoretical works of binary formation. Such kind of the information involves the mass ratio and the evolutionary difference of the binary, the size and the mass of circumstellar disk around each star, and the spatial relation between the plane of the binary orbit and that of the circumstellar disks. In this thesis, we try to understand spatial and velocity structures of gas and dust around the protostellar binary IRAS 16293-2422 using the Nobeyama Millimeter Array, and to get information leading to an implication for binary formation and evolution.

The outline of this thesis is as follows. In §2 we will describe the observations. The results of mapping observations toward IRAS 16293-2422 will be presented in §3. Summary of the results will be appeared in §4. The kinematical structure of molecular gas around source A will be discussed in §5. In §6 we will present the interpretation of the structure and evolution of the binary system. In §7 the relation between outflow phenomena and the binary system will be mentioned.

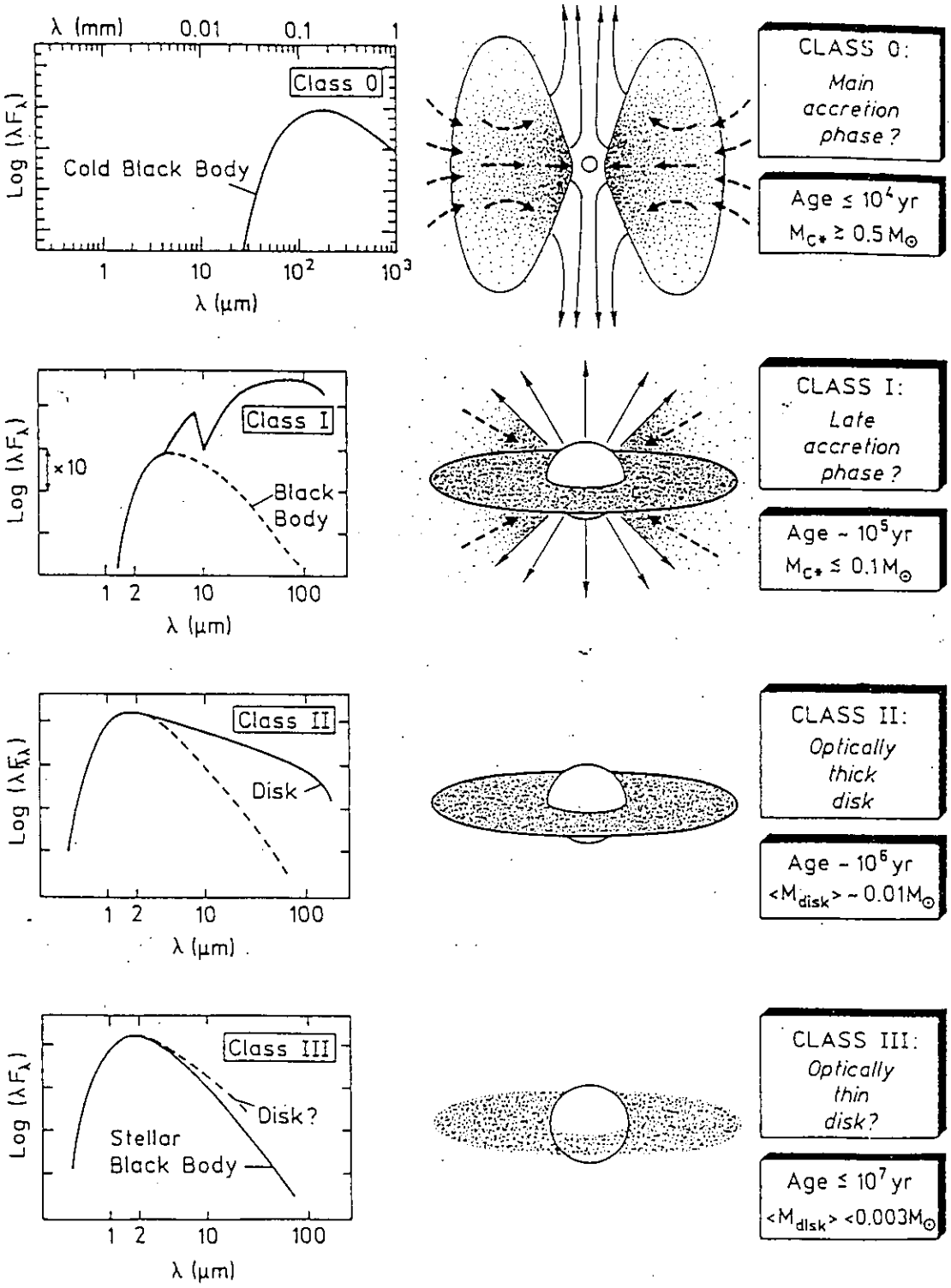

Figure 1.1. Quasi-continuous evolutionary sequence of SEDs for low-mass YSOs from Andre (1994).

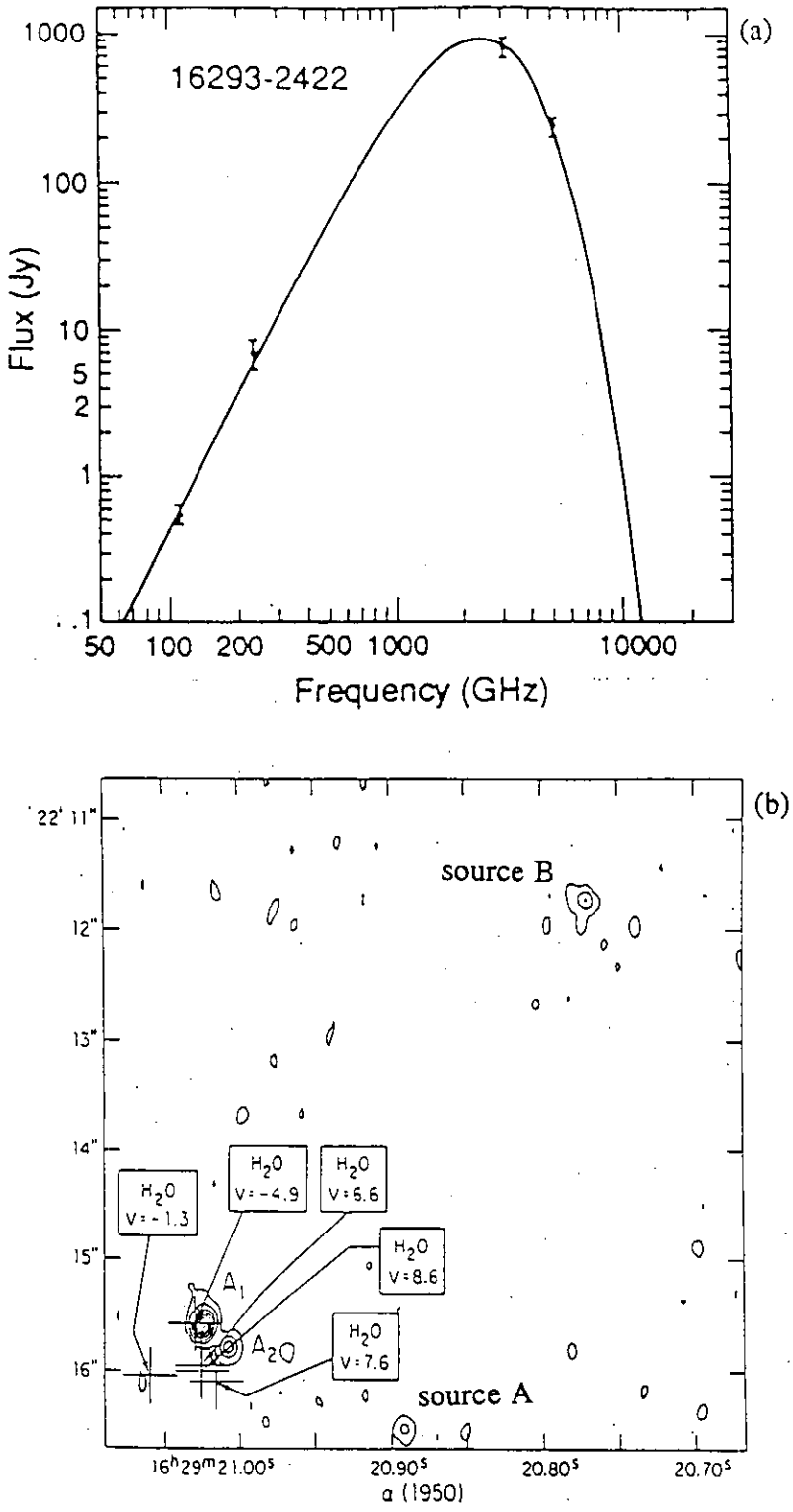

Figure 1.2. (a) Far-infrared spectral energy distribution of IRAS 16293-2422 from Walker *et al.* (1990). The fitted curve is expressed of the form, $F_\nu = \Omega_s B_\nu(T)(1 - e^{-\tau_\nu})$ ($\tau_\nu = (\nu/\nu_0)^\beta$), where $\Omega_s = 2.67 \times 10^{-9}$, $T = 35$ K and $\beta = 1.27 \pm 0.12$. (b) Detail of the 2 cm continuum emission at IRAS 16293-2422 sources A and B, where source A is resolved into components A1 and A2, and the location of the H_2O masers obtained using the VLA from Wootten (1989). Contours are drawn at intervals of 3, 6, 9, 12, 15, 18, 21, 24, 27, and 30 times the rms noise level of map, which is 70 μJy.

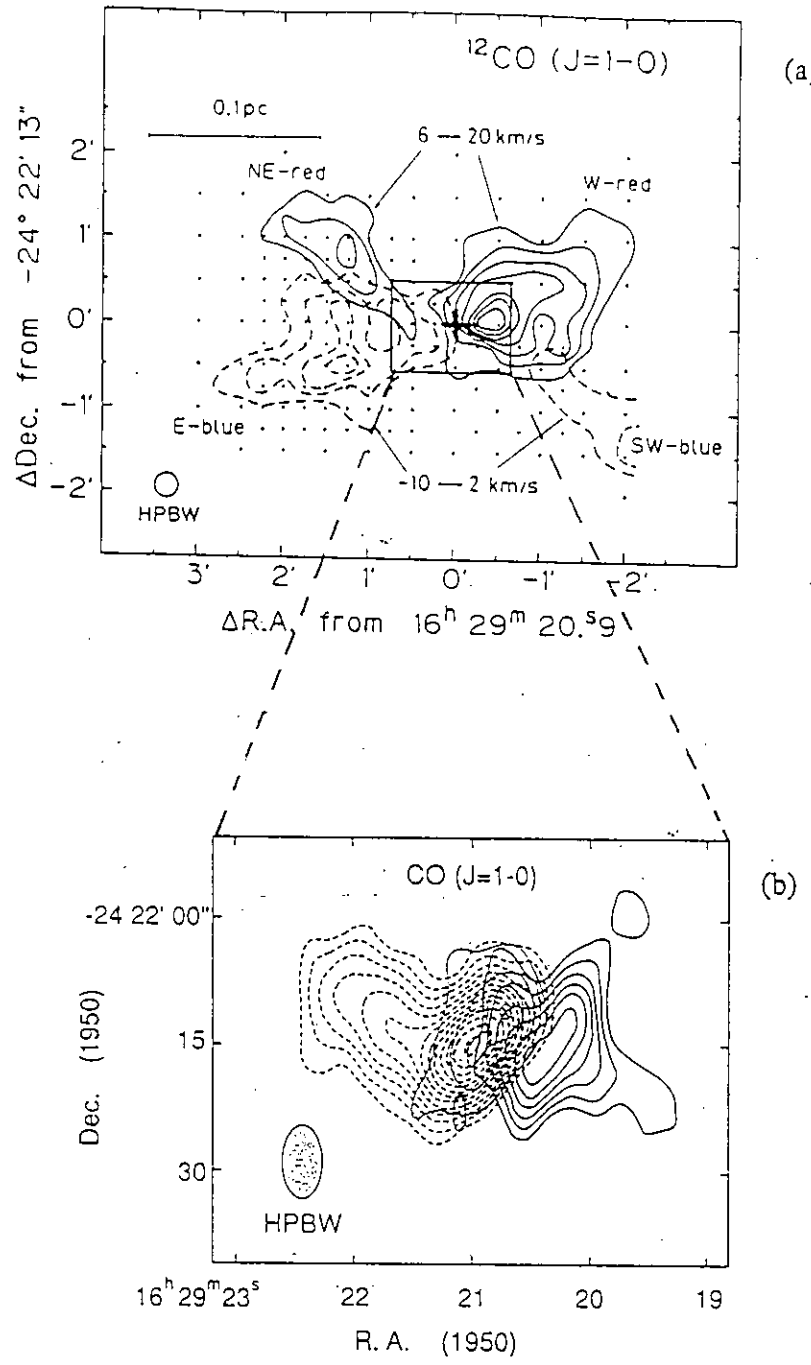

Figure 1.3. (a) Distribution of the high-velocity CO $J = 1 - 0$ emission in IRAS 16293-2422 obtained with the Nobeyama 45 m telescope from Mizuno *et al.* (1990). The integrated intensity of the redshifted wing is shown by solid contours and that of the blueshifted wing is shown by dashed contours. Contours are every 5.4 K km s^{-1} from 10.8 K km s^{-1} . The position of an IRAS point source (IRAS 16293-2422) is denoted by a cross. (b) Interferometric CO map of IRAS 16293-2422 taken with the Nobeyama Millimeter Array is superposed on the 2.7 mm continuum interferometric map of Mundy *et al.* (1986). The velocity intervals are -0.4 to -3.6 km s^{-1} (dashed contours) and 8.5 to 12.5 km s^{-1} (solid contours). The contours extend from 2σ rms noise level with a 1σ step. The 1σ rms noise level is 70 mJy beam^{-1}. (from Fukui *et al.* 1994).

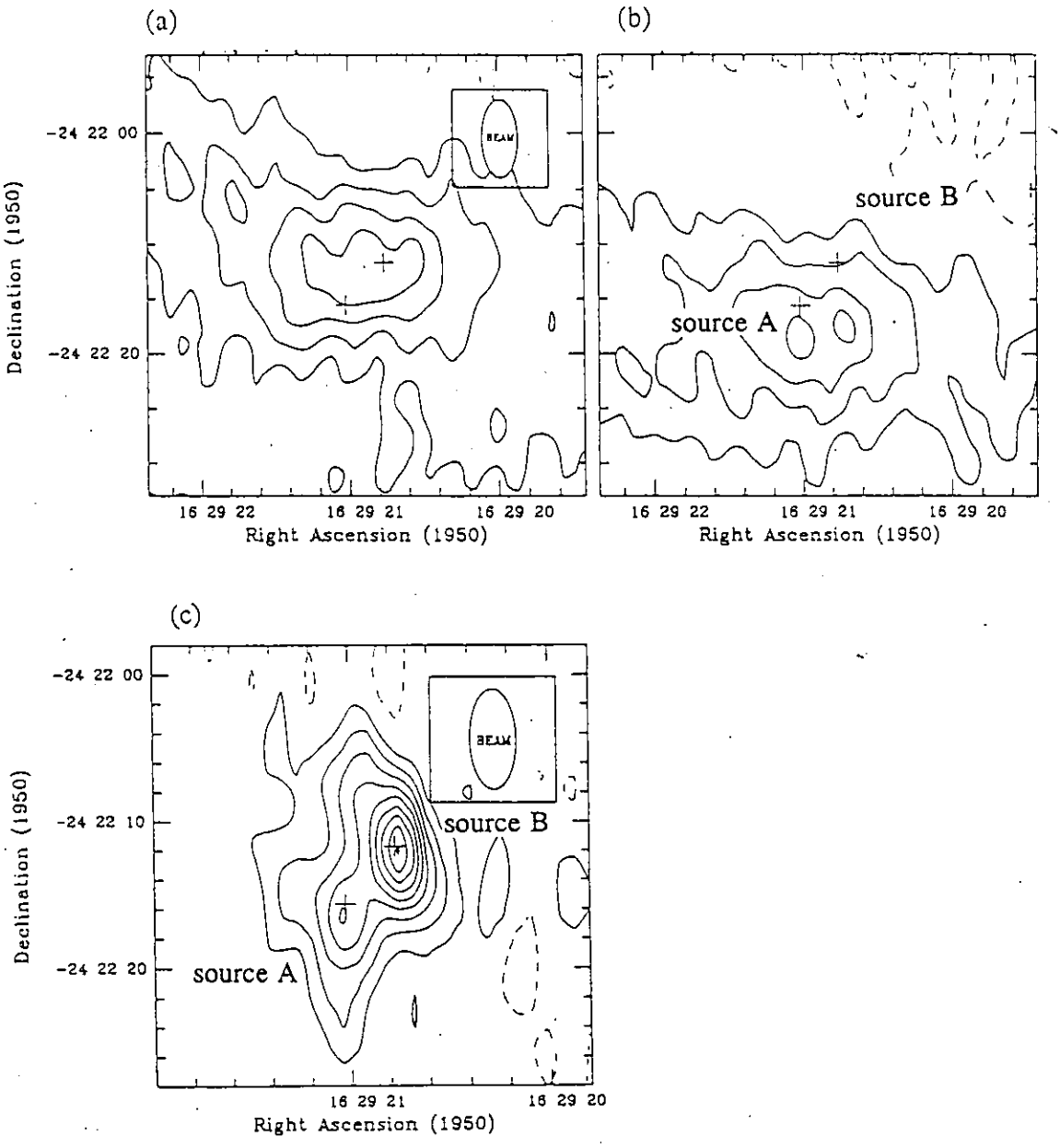

Figure 1.4. (a), (b) Interferometer maps toward IRAS 16293-2422 of the CS $J = 2 - 1$ emission integrated over (a) from V_{LSR} = 1.75 to 3.25 km s^{-1} , and (b) from 6.25 to 9.,25 km s^{-1} . The contours are integer multiples of 7.6 K km s^{-1} starting at $\pm$ 7.6 K km s^{-1} , and the noise level is 2.5 K km s^{-1} . (c) Interferometer map of the 3 mm continuum emission. The contours are integer multiples of 26 mJy starting at 26 mJy. The VLA positions of the centimeter-wave emission are indicated by crosses. The FWHM of the synthesized beam is shown in the top right corner of the figure. The noise level is 17 mJy $beam^{-1}$. (a)-(c) are obtained using the Hat Creek Millimeter array from Walker *et al.* (1993).

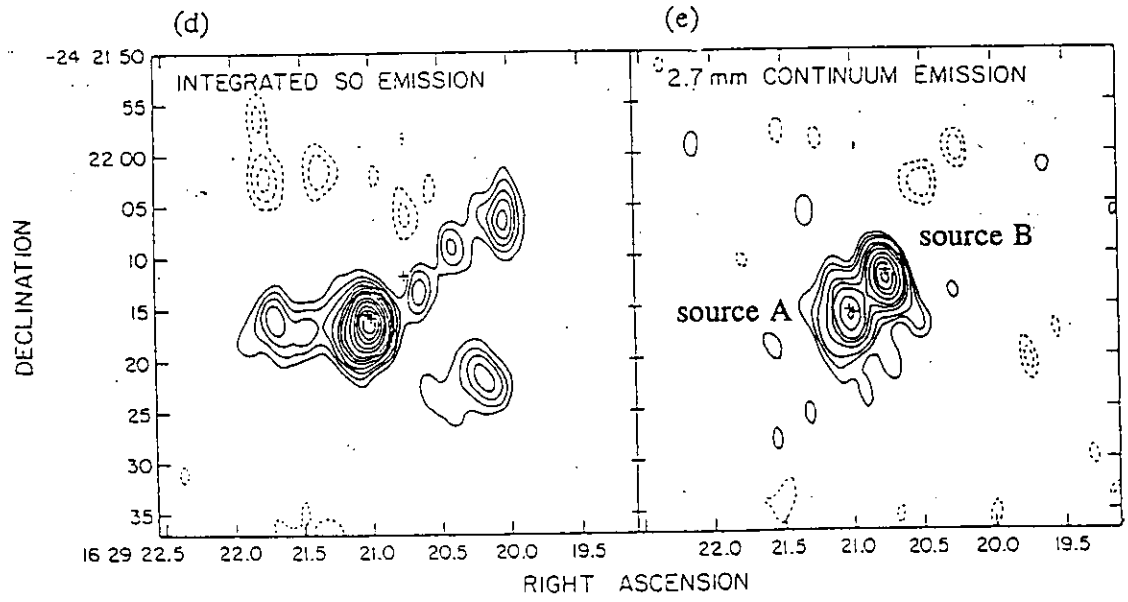

Figure 1.4. (d) Integrated SO $J = 2,3 - 2,1$ line emission. The contours are -4, -3, -2,2,3,4,5,6,7,8,9,10,12,14,16, and 18 times 0.37 Jy beam^{-1} km s^{-1} . (e) 2.75 mm continuum emission. The contours are -4,-2,2,4,6,8,10,12,14,18,22,26,and 30 times 7.5 mJy beam^{-1}. (d)-(e) are obtained using OVRO Millimeter Wave Interferometer from Mundy *et al.* (1992).

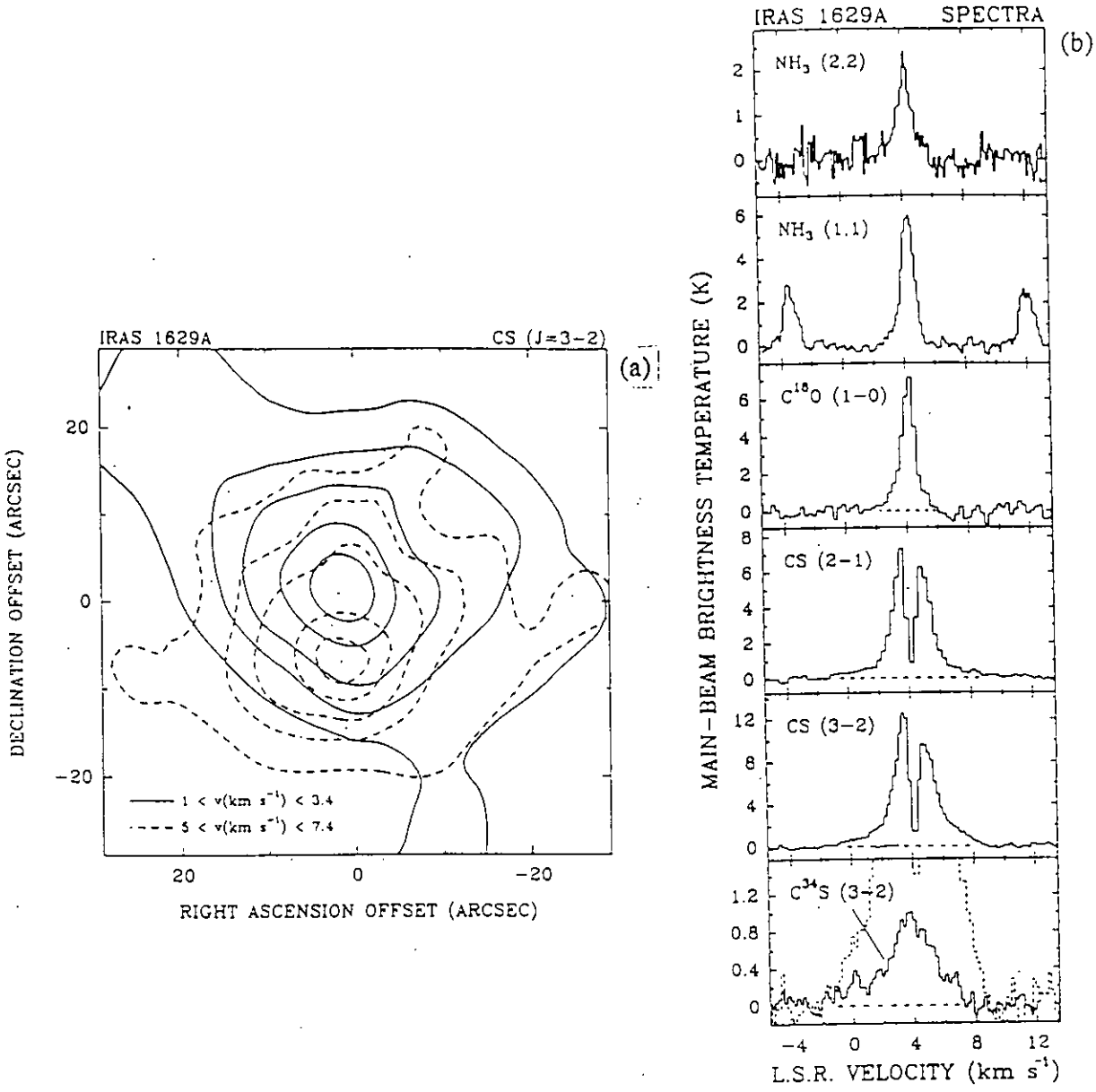

Figure 1.5. (a) Velocity-integrated $C^{32}S$ $J = 3 - 2$ emission obtained using the IRAM 30 m dish from Menten (1987). Offsets relative to the position of the IRAS point source (IRAS 16293-2422). Contours represents 25,45,65,85, and 95 % levels of the peak value which is 10.0 K km s^{-1} for the blue- and 11.5 K km s^{-1} for redshifted component. These velocity intervals are selected to exclude the absorbing layer. (b) NH_3, $C^{18}O$ and CS spectra toward IRAS 16293-2422 obtained using the IRAM 30 m dish from Menten (1987). In the lowest panel, the $C^{32}S$ $J = 3 - 2$ line (dashed) is superposed on the $C^{34}S$ $J = 3 - 2$ line for comparison.

2 Observations

$C^{32}S$ $J = 3-2$, $C^{32}S$ $J = 2-1$ and $C^{34}S$ $J = 2-1$ toward IRAS 16293-2422 were observed with the Nobeyama Millimeter Array. The phase center of the observations was selected at the IRAS point source catalog position ($\alpha(1950) = 16^h29^m20^s.9$, $\delta(1950) = -24°22'13''.0$). The array consists of five 10 m antennas which are equipped with SIS receivers with a fixed tuning mixer (Sunada *et al.* 1993). The system noise temperatures at the zenith were approximately 500 K (DSB) for $C^{32}S$ $J = 3-2$, 300 K (DSB) for $C^{32}S$ $J = 2-1$ and 50 K (DSB) for $C^{34}S$ $J = 2-1$. An FFT spectro-correlator (FX) with 1024 velocity channels (Chikada *et al.* 1987) was used. The bandwidth was 320 MHz, and the corresponding velocity resolution are shown in Table 2.1. The line-free channels were used for mapping both 98 GHz and 147 GHz continuum emissions.

For $C^{32}S$ $J = 3-2$ and $C^{32}S$ $J = 2-1$ the observations were carried out with three array configurations and for $C^{34}S$ $J = 2-1$ with two configurations. The minimum and maximum projected baseline lengths were 12 m and 280 m, respectively, for $C^{32}S$ $J = 3-2$ and $C^{32}S$ $J = 2-1$, and 10 m and 150 m, respectively, for $C^{34}S$ $J = 2-1$. Therefore, our observations were insensitive to the extended structures larger than $38''$ for $C^{32}S$ $J = 3-2$, $60''$ for $C^{32}S$ $J = 2-1$ and $32''$ for $C^{34}S$ $J = 2-1$. The synthesized beam size and the primary beam size are shown in Table 2.1 and Table 2.2.

NRAO530 was observed every 40 minutes for 10 minutes during the observations to calibrate the instrumental gain and phase. The variation of the flux density of NRAO530 was determined from observations of Uranus whose brightness temperature at 98 GHz and at 147 GHz were assumed to be 130 K and 114 K, respectively. The derived flux densities of NRAO530 were shown in Table 2.1 and Table 2.2. The bandpass calibration of the complex visibilities was made from the observations of 3C273 for $C^{32}S$ $J = 3-2$ and $C^{32}S$ $J = 2-1$, and 3C454.3 for $C^{34}S$ $J = 2-1$. Maps were constructed using the CLEAN algorithm provided by NRAO AIPS package. To improve sensitivity, the $C^{32}S$ $J = 3-2$ map was made with 100 kλ u-v Gaussian taper and the $C^{34}S$ $J = 2-1$ map with 30 kλ u-v Gaussian taper. The derived synthesized beam size and the primary beam size are shown in Table 2.1 and Table

2.2.

The absolute positional error in the maps is less than 10% of each synthesized beam, and the relative positional accuracy between the CS and the continuum maps is better than $0''.5$. The uncertainty of their flux density scale is 15%. The rms noise levels of the maps are shown in Table 2.1 and Table 2.2.

Table 2.1 Observational parameters of CS emissions

	$C^{32}S$ $J = 3 - 2$	$C^{32}S$ $J = 2 - 1$	$C^{34}S$ $J = 2 - 1$
Date	February-April 1992	February-April 1992	December 1994-April 1995
Center Frequency (GHz)	146.969039	97.980968	96.412982
Velocity Resolution (km s^{-1})	0.64	0.96	0.97
Synthesized Beam ($''\times\ ''(°)$)	4.2 × 2.6 (0.8)	5.3 × 3.3 (3.8)	11.8 × 6.6 (11.9)
Primary beam ($''\times\ ''$)	50	75	75
Bandpass Calibrator	3C273	3C273	3C454.3
Reference Calibrator	NRAO530	NRAO530	NRAO530
Calibrator flux (Jy)	5.5	3.4	9.5
Noise Level (K)	2.7	1.5	0.16

Table 2.2 Observational parameters of continuum emissions

	98 GHz (λ3 mm)	150 GHz (λ2mm)
Date	February-April 1992	February-April 1992
Synthesized Beam ($''\times\ ''(°)$)	5.2 × 3.1 (5.9)	3.3 × 2.0 (3.7)
Primary beam ($''\times\ ''$)	75	50
Bandpass Calibrator	3C273	3C273
Reference Calibrator	NRAO530	NRAO530
Calibrator flux (Jy)	3.4	5.5
Noise Level (mJy/beam)	6.6	20

3 Results

3.1 $C^{32}S$ $J = 2 - 1$, $C^{32}S$ $J = 3 - 2$ and $C^{34}S$ $J = 2 - 1$ emission

3.1.1 Channel maps and total integrated intensity maps

Figure 3.1 shows velocity channel maps of $C^{32}S$ $J = 2 - 1$ emission for velocities from V_{LSR} = -0.67 to 8.89 km s^{-1} together with a map of the total $C^{32}S$ $J = 2 - 1$ intensity integrated over the velocity range from V_{LSR} = -0.67 to 7.93 km s^{-1} . Figure 3.2 also shows velocity channel maps of $C^{32}S$ $J = 3 - 2$ (V_{LSR} = -1.46 to 10.02 km s^{-1}) and an integrated intensity map of $C^{32}S$ $J = 3 - 2$ (V_{LSR} = -1.46 to 7.47 km s^{-1}). In these Figures, the positions of the 2 cm continuum sources A and B (Wootten 1989) are shown by crosses. The $C^{32}S$ $J = 2 - 1$ emission was detected over 4 σ noise level at V_{LSR} = 0.28 to 6.98 km s^{-1} and the emission at V_{LSR} = -0.67 and 7.93 km s^{-1} was marginally detected. The $C^{32}S$ $J = 3 - 2$ emission was detected over 4 σ noise level at V_{LSR} = 1.73 to 6.19 km s^{-1} .

As seen from Figures 3.1 and 3.2, the emissions become weaker at V_{LSR} = 4.11 km s^{-1} for the $C^{32}S$ $J = 2 - 1$ and at V_{LSR} = 4.28 km s^{-1} for the $C^{32}S$ $J = 3 - 2$. These velocities correspond to those of the self absorption feature seen at the systemic velocity of the parent molecular cloud core, which is $V_{LSR} \sim 4$ km s^{-1} , as mentioned in section 1.3. Thus the features that the CS emissions become weaker at $V_{LSR} \sim 4$ km s^{-1} in our maps are interpreted to be caused due to the self-absorption.

In Figure 3.1 the emission toward source A is detected for all velocity channels except for V_{LSR} = 8.89 km s^{-1} . The main features around source A is as follows: (1) The $C^{32}S$ $J = 2 - 1$ emissions are located on the north side of source A from V_{LSR} = 2.19 to 3.15 km s^{-1} , while on the south side of source A from V_{LSR} = 5.06 to 7.93 km s^{-1} , (2) EW elongation of molecular gas was found at V_{LSR} = 5.06 and 6.02 km s^{-1} and seems to be associated with source A, and (3) The $C^{32}S$ $J = 2 - 1$ emissions are tightly associated with source A from V_{LSR} = -0.67 to 1.24 km s^{-1} . Of the three features the NS velocity shift of molecular gas and the EW elongation of molecular gas are also seen in the $C^{32}S$ $J = 2 - 1$ maps obtained by Walker *et al.* (1992). However the center of the NS velocity shift is not

clear in their maps. We will mention about the features, (1), (2), and (3) in section 3.1.4, 3.1.5, and 3.1.8.

In Figure 3.1 there exists the molecular gas closely associated with source B at V_{LSR} = 2.19 and 3.15 km s^{-1} (only two of the channel maps). Except for this feature, there is no emission just centered on source B. We will mention about this in section 1.6.

The gas distribution of the $C^{32}S$ $J = 3 - 2$ are roughly the same as that of the $C^{32}S$ $J = 2 - 1$.

Figure 3.3 shows velocity channel maps of $C^{34}S$ $J = 2 - 1$ emission for velocities from V_{LSR} = 1.26 to 8.06 km s^{-1} together with a map of the total $C^{34}S$ $J = 2 - 1$ intensity integrated over the velocity range from V_{LSR} = 1.26 to 8.06 km s^{-1} . The $C^{34}S$ $J = 2 - 1$ emission was detected over 4 σ noise level at V_{LSR} = 2.23, 3.20 and 5.15 km s^{-1} and the self absorption feature is not so clear as seen in the $C^{32}S$ maps.

The total integrated intensities of $C^{32}S$ $J = 2 - 1$, $C^{32}S$ $J = 3 - 2$ and $C^{34}S$ $J = 2 - 1$ emissions (Figs. 3.1*l*, 3.2*t* and 3.3*i*) all peak at the position of source A. The spatial distribution of the total $C^{32}S$ $J = 3 - 2$ emission (Fig. 3.2*t*) mimics that of the total $C^{32}S$ $J = 2 - 1$ emission (Fig. 3.1*l*) except that the elongation of the $C^{32}S$ $J = 3 - 2$ emission toward the position of source B is clearly seen. The spatial distribution of the total $C^{34}S$ $J = 2 - 1$ emission (Fig. 3.3*i*), however, is different from that of the $C^{32}S$ emissions and shows an elongated structure centered at source A. Total flux densities integrated over the CS maps are 45 $\pm$ 6.8 Jy km s^{-1} , 280 $\pm$ 42 Jy km s^{-1} , and 4.0 $\pm$ 0.6 Jy km s^{-1} for $C^{32}S$ $J = 2 - 1$, $C^{32}S$ $J = 3 - 2$, and $C^{34}S$ $J = 2 - 1$, respectively. It should be noted that these flux densities originate from the compact structure, since the interferometric observation misses an emitting flux from extended structure. By comparing the flux densities of our maps with those obtained with the IRAM 30 m dish by Menten *et al.* (1987) and the NRO 45 m dish by Mikami *et al.* (1995), the amount of the missing fluxes for the $C^{32}S$ $J = 2 - 1$ and $C^{32}S$ $J = 3 - 2$ emissions are estimated to be 70 - 80 % of the emissions from the extended structure. On the other hand, the $C^{34}S$ $J = 2 - 1$ emission is scarcely missed, and the missing flux is only 3 %. It means that the distribution of the $C^{34}S$ emission is originally more compact than that of $C^{32}S$.

3.1.2 $C^{32}S$ blue- and redshifted emissions

To illustrate velocity structure of the $C^{32}S$ emission clearly we hereafter define blue- and redshifted components based on the velocities of self absorption features: 4.11 km s^{-1} for $C^{32}S$ $J = 2 - 1$ and 4.28 km s^{-1} for $C^{32}S$ $J = 3 - 2$. The blueshifted component is defined as that integrated over the velocity range from V_{LSR} = 2.19 to 3.15 km s^{-1} for $C^{32}S$ $J = 2 - 1$ (Figs. 3.1*d*-*e*) and from V_{LSR} = 2.36 to 3.64 km s^{-1} for $C^{32}S$ $J = 3 - 2$ (Figs. 3.2*g*-*i*), and redshifted one as that from V_{LSR} = 5.06 to 6.02 km s^{-1} for $C^{32}S$ $J = 2 - 1$ (Figs. 3.1*g*-*h*) and from V_{LSR} = 4.92 to 6.19 km s^{-1} for $C^{32}S$ $J = 3 - 2$ (Figs. 3.2*k*-*m*), so as to obtain the same velocity width for each component: 1.91 km s^{-1} .

The $C^{32}S$ blueshifted emissions (Figs. 3.4*a* and *c*) has two peaks - one is associated with source A and the other with source B - while the $C^{32}S$ redshifted emissions (Figs. 3.4*b* and *d*) has only one peak in the vicinity of source A. Integrated flux densities of the CS emission associated with each source are evaluated from a two-dimensional Gaussian fit to each peak. These values are listed in Table 3.2.

3.1.3 $C^{34}S$ disk-like structure around source A

To illustrate the elongated structure seen in the total $C^{34}S$ map (Fig 3.3*i*) Figure 3.5 shows the $C^{34}S$ $J = 2 - 1$ emission integrated over from V_{LSR} = 2.23 to 5.15 km s^{-1} . The $C^{34}S$ emissions show elongated disk-like structure around source A. A FWHM size of the disk-like structure is $20'' \times 8''.4$ corresponding to 3200 AU $\times$ 1300 AU, though the length of the minor axis is uncertain because of contamination of the emission associated with source B. A position angle of the major axis of the disk-like structure is $\sim 30°$, which is close to (1) the axis connecting the centimeter emission sources A1 and A2 (Wootten 1989, see also Fig. 1.2.(b)), and (2) the magnetic field direction in the vicinity of IRAS 16293-2422 inferred from the millimeter polarimetry (Tamura *et al.* 1993), while roughly perpendicular to (1) the axis connecting the binary sources A and B, and (2) the direction of the E-blue and the W-red lobes of the molecular outflow (Mizuno *et al.* 1990).

This elongation is also found in the blueshifted components of the $C^{32}S$ $J = 2 - 1$ (Fig.

3.4*a*) and $J = 3 - 2$ emissions (Fig. 3.4*c*) and slightly found in the redshifted components of the $C^{32}S$ $J = 2 - 1$ emission (Fig. 3.4*b*). Thus the disk-like structure is suspected to be a denser part traced more clearly by the optically thin $C^{34}S$ emission. Being perpendicular to the the outflow axis as mentioned above, the elongated disk-like structure is interpreted naturally to be a gaseous disk around source A.

The gaseous disk was expected to exist, because the centimeter continuum emission of sources A1 and A2 is interpreted to arise from a warm shocked region at the interface of a neutral stellar wind and the ambient dense gas (Wootten 1989), tracing the inner part of the gaseous disk or torus. A similar phenomenon is reported in the case of L1551 IRS 5 (Rodriguez *et al.* 1986). The exciting protostar is suggested to be located between the two radio sources A1 and A2. Thus the disk-like structure observed by the $C^{34}S$ $J = 2 - 1$ emission should be the outer part of the gaseous disk.

The $C^{34}S$ $J = 2 - 1$ emissions associated with each source are not clearly distinguished because of poor angular resolution. To estimate the flux densities of the $C^{34}S$ $J = 2 - 1$ emission associated with each source we divide the $C^{34}S$ emissions into two portions on each side of a line, whose position angle is 30°, drawn through a midpoint between sources A and B. The flux density of the disk around source A is estimated to be 3.3 ± 0.5 Jy and that of the $C^{34}S$ gas associated with source B is to be 0.7 ± 0.1 Jy.

3.1.4 Velocity structure around source A: rotating disk around source A

In the maps of the blue- and redshifted $C^{32}S$ $J = 2 - 1$ and $C^{32}S$ $J = 3 - 2$ emission there is a systematic velocity gradient about the systemic velocity along the N-S direction just around source A: *i.e.*, the blueshifted emission is located in the north side of source A (Figs. 3.4*a* and *c*) while the redshifted emission in the south side (Figs. 3.4*b* and *d*).

In the $C^{34}S$ $J = 2 - 1$ channel maps (Figure 3.3) there is a little velocity shift along the major axis of the elongated disk-like structure around source A: *i.e.*, the blueshifted emission at $V_{LSR} = 3.20$ km s^{-1} is located at the NE side of source A while the redshifted one at $V_{LSR} = 4.17$ km s^{-1} at the SW side of source A. The trend of the velocity gradient seen in the $C^{34}S$ $J = 2 - 1$ emissions is almost the same as that seen in $C^{32}S$ $J = 2 - 1$ and $J = 3 - 2$

emissions. Thus the velocity shift seen in $C^{32}S$ may arise in the disk-like structure around source A.

To illustrate the gas kinematics more clearly, we show the position-velocity maps of the CS emission cutting along the major axis of the disk-like structure through source A (the cutting line M-M' in Figure 3.5) in Figure 3.6 for $C^{32}S$ and in Figure 3.7 for $C^{34}S$. The solid lines show the position of source A. The $C^{32}S$ $J = 2 - 1$ and $J = 3 - 2$ velocity structures are well explained with the rotating molecular gas around source A. The main arguments for this interpretation are as follows: (1) The appearances of the position-velocity maps are nearly symmetric about the position of source A and the systemic velocity of 4 km s^{-1} . (2) In the outer region (offset $> 10''$) the velocity gets closer to the systemic velocity, though the emissions at the redshifted side is not seen. At the velocity extremes the emission is compact and the peaks of CS emission are very close to the position of source A. The position-velocity map of the $C^{34}S$ $J = 2 - 1$ emission (Figure 3.7) resembles a low resolution version of that of the $C^{32}S$ $J = 2 - 1$ emission.

The diameter of the rotating gas, estimated from the FWHM of the blue- and the redshifted components on the $C^{32}S$ $J = 2 - 1$ position-velocity map (Figure 3.6), is $14''.1$, which corresponds to 2260 AU at the distance of 160 pc. The velocity shift within 2260 AU is $\sim$ 2.0 km s^{-1} .

Walker *et al.* (1993) claimed in their interferometric observations of the $C^{32}S$ $J = 2 - 1$ emission toward IRAS 16293-2422 that the molecular gas is rotating around the binary system, *i.e.*, forms the circumbinary structure. It becomes, however, clear in our $C^{32}S$ $J = 2 - 1$ and $C^{32}S$ $J = 3 - 2$ maps that the molecular gas is rotating around source A forming the circumstellar structure, in other word, the kinematical center of the molecular gas is located at source A.

3.1.5 EW elongation around source A

EW elongation of molecular gas was found in both the $C^{32}S$ $J = 2 - 1$ and $J = 3 - 2$ maps at $V_{LSR} \sim 5$ km s^{-1} and seems to be associated with source A. The flux density of the EW elongation is 8.4 $\pm$ 1.3 Jy and 41 $\pm$ 7.7 Jy for $C^{32}S$ $J = 2 - 1$ and $J = 3 - 2$, respectively.

The EW elongation has length of $\sim$ 29″, which corresponds to 4600 AU at the distance of 160 pc, and probably extends outside of the field of view (F.O.V) of the observations. The direction of the elongation is roughly coincident with the direction of brighter one of two outflows (PA=110°), but the relative velocity of the molecular gas to the systemic velocity is as small as $\sim$1 km s^{-1} . Then, this molecular gas would not be a part of the molecular outflow but possibly the ambient molecular gas compressed and accelerated by the interaction with the outflow.

3.1.6 Molecular gas associated with source B

The molecular gas was found to exist closely associated with source B at V_{LSR} = 2.19 and 3.15 km s^{-1} in $C^{32}S$ $J = 2 - 1$ channel maps and V_{LSR} = 3.00 and 3.64 km s^{-1} in $C^{32}S$ $J = 3 - 2$. These emissions are clearly seen on the maps of the blueshifted emission (Figures 3.4 (a) and (c)). Except for this feature, there is no $C^{32}S$ $J = 2 - 1$ and $J = 3 - 2$ emission just centered on source B. Flux density of the emissions associated with source B is estimated to be 10.2 $\pm$ 2.3 Jy and 90.5 $\pm$ 20.4 Jy for $C^{32}S$ $J = 2 - 1$ and $J = 3 - 2$, respectively.

3.1.7 $C^{32}S$ $J = 3 - 2$ / $C^{32}S$ $J = 2 - 1$ intensity ratio

In the blueshifted $C^{32}S$ emissions (Figures 3.4 (a) and (c)) the peak in the vicinity of source A is stronger than that near source B in the $C^{32}S$ $J = 2 - 1$ map, while it is weaker in the $C^{32}S$ $J = 3 - 2$ map. This means that the $C^{32}S$ $J = 3 - 2$ / $C^{32}S$ $J = 2 - 1$ intensity ratio of the blueshifted emission associated with source B is higher than that of source A. The $C^{32}S$ $J = 3 - 2$ / $C^{32}S$ $J = 2 - 1$ intensity ratios evaluated using the beam matched (6″) maps are given in Table 3.2. It is, however, noted that it is difficult to obtain a definite value of the intensity ratio because of the following reasons; 1) The u-v coverage differs between the observing frequencies: the spatial frequencies sampled with the $C^{32}S$ $J = 3 - 2$ observations correspond to the range from 1″.6 to 38″ in image domain, while that with the $C^{32}S$ $J = 2 - 1$ observations correspond to from 2″.5 to 60″. 2) The amount of the self-absorption may be different between the $C^{32}S$ $J = 3 - 2$ and the $C^{32}S$ $J = 2 - 1$ emissions. 3) The systemic velocity of each source may differ: the center velocity of source B is about 3 km s^{-1} , while

that of source A is about 4 km s^{-1} , the same as that of the core. Thus the intensity ratio toward source B involves considerable uncertainties, however, there is a possibility that the higher $C^{32}S$ $J = 3 - 2$ / $C^{32}S$ $J = 2 - 1$ intensity ratio of the gas associated with source B would imply higher temperature or higher H_2 gas density of the molecular gas associated with source B. We need further observations to ascertain it.

3.1.8 Blueshifted wing emission associated with source A

The channel maps (Figures. 3.1 and 3.2) suggest the presence of a blueshifted wing emission component. In order to illustrate this wing emission clearly, we show in Figure 3.8 the maps of the blueshifted wing emission integrated over three velocity channels in the $C^{32}S$ $J = 2 - 1$ (Figures. 3.1*a*-*c*) and over five channels in the $C^{32}S$ $J = 3 - 2$ (Figures. 3.2*a*-*e*). The wing emission is detected above 9 σ noise level in the $C^{32}S$ $J = 2 - 1$ map and above 5 σ noise level in the $C^{32}S$ $J = 3 - 2$. The wing emissions are tightly associated with source A, and are not resolved by our beam sizes. On the other hand, there is no corresponding emission at the redshifted side. Flux density of the blueshifted wing emissions associated with source A is estimated to be 3.8 $\pm$ 1.3 Jy km s^{-1} and 16 $\pm$ 4.6 Jy km s^{-1} for $C^{32}S$ $J = 2 - 1$ and $J = 3 - 2$, respectively.

3.1.9 Mass estimation from the CS emissions

The flux densities of the CS emission would trace the molecular gas mass. The optically thin $C^{34}S$ emission is a better tracer of high density regions near the protostars, although the derived gas mass from $C^{32}S$ emissions are presumably a lower limit. The gas mass is estimated with the assumptions of optically thin LTE conditions using the following equations: from the total flux densities of the $C^{32}S$ $J = 2 - 1$ emission,

$$M = 4.7 \times 10^{-17} \frac{1}{X(\mathrm{C^{32}S})} \frac{\exp(2.4/T)}{1 - \exp(-4.7/T)} \left(\frac{D}{\mathrm{pc}}\right)^2 \left(\frac{F_\nu \, \Delta V}{\mathrm{Jy\ km\ s^{-1}}}\right) M_\odot, \qquad (1)$$

from that of the $C^{32}S$ $J = 3 - 2$ emission,

$$M = 1.2 \times 10^{-17} \frac{1}{X(\mathrm{C^{32}S})} \frac{\exp(7.1/T)}{1-\exp(-7.1/T)} \left(\frac{D}{\mathrm{pc}}\right)^2 \left(\frac{F_\nu\ \Delta V}{\mathrm{Jy\ km\ s^{-1}}}\right) M_\odot, \quad (2)$$

and from that of the $C^{34}S$ $J = 2-1$ emission,

$$M = 4.9 \times 10^{-17} \frac{1}{X(\mathrm{C^{34}S})} \frac{\exp(2.3/T)}{1-\exp(-4.6/T)} \left(\frac{D}{\mathrm{pc}}\right)^2 \left(\frac{F_\nu\ \Delta V}{\mathrm{Jy\ km\ s^{-1}}}\right) M_\odot, \quad (3)$$

where $X(\mathrm{CS})$ is the fractional CS abundance, T is the gas excitation temperature, D is the distance to the CS source, and $F_\nu\ \Delta V$ is the total flux density.

For IRAS 16293-2422 Menten *et al.* (1987) derived $X(\mathrm{CS})$ to be $\sim 3.7 \times 10^9$ and T to be ~ 40 K from a multitransitional LVG analysis. Walker *et al.* (1990) estimated $X(\mathrm{CS})$ to be $\sim 4 \times 10^9$ from a comparison between the column densities. First they estimated an abundance ratio of [CS]/[^{13}CO] to be 1.6×10^{-3} from their observations, and then they derived $X(\mathrm{CS})$ by combining their result with the [^{13}CO]/[H_2] ratio of 2.5×10^{-6} determined by Dickman (1987). Hence we assumed $X(\mathrm{C^{32}S})$ to be 4×10^{-9} (Menten *et al.* 1987; Walker *et al.* 1990), the $^{32}S/^{34}S$ abundance to be terrestrial, or 22.5, and the gas excitation temperature T to be 40 K (Menten *et al.* 1987; Blake *et al.* 1994). The estimated gas masses are listed in Table 3.1, Table 3.2 and Table3.3.

It is clear that about 70 % of the molecular gas are associated with source A. Thus the center of the mass is source A.

The gas mass evaluated from the $C^{34}S$ $J = 2-1$ emission of $0.27 \pm 0.041\ M_\odot$ is consistent with that of $0.22\ M_\odot$ estimated from the total flux density of $C^{18}O$ emission by Mundy *et al.* (1990).

Table 3.1 Derived quantities of CS integrated intensities

	$C^{32}S$ $J = 3 - 2$	$C^{32}S$ $J = 2 - 1$	$C^{34}S$ $J = 2 - 1$
total flux density (Jy km s^{-1})	280 ± 42	45.3 ± 6.8	4.0 ± 0.6
missing flux (%)[a]	70	81	3
$M(H_2)$ ($M_\odot$)[b]	0.16 ± 0.025	0.12 ± 0.017	0.27 ± 0.041

a. comparing the flux densities of our maps with those obtained using IRAM 30 m dish by Menten *et al.* (1987) in the case of $C^{32}S$ $J = 3 - 2$ and $C^{32}S$ $J = 2 - 1$, and with those obtained using NRO 45 m dish by Mikami *et al.* (1995) in the case of $C^{34}S$ $J = 2 - 1$.

b. assuming a fractional $C^{32}S$ abundance of 4×10^{-9} (Menten *et al.* 1987; Walker *et al.* 1990), a terrestrial $^{32}S/^{34}S$ abundance of 22.5 and a gas kinetic temperature of 40 K (Menten *et al.* 1987) with optically thin LTE conditions.

Table 3.2 Derived quantities of $C^{32}S$ blue- and redshifted emissions

	source A	source B
integrated flux of CS emission (Jy km s^{-1}) [a]		
$C^{32}S$ $J = 2 - 1$ blue	10.3 ± 2.6	10.2 ± 2.3
$C^{32}S$ $J = 2 - 1$ red	18.6 ± 4.0	
$C^{32}S$ $J = 2 - 1$ blue-wing	3.79 ± 1.25	
$C^{32}S$ $J = 3 - 2$ blue	36.3 ± 9.5	90.5 ± 20.4
$C^{32}S$ $J = 3 - 2$ red	130.3 ± 27.4	
$C^{32}S$ $J = 3 - 2$ blue-wing	16.1 ± 4.6	
$M(H_2)$ ($M_\odot$) [b]		
$C^{32}S$ $J = 2 - 1$ blue	0.027 ± 0.004	0.026 ± 0.004
$C^{32}S$ $J = 2 - 1$ red	0.048 ± 0.007	
$C^{32}S$ $J = 2 - 1$ blue-wing	0.010 ± 0.002	
$C^{32}S$ $J = 3 - 2$ blue	0.020 ± 0.003	0.051 ± 0.008
$C^{32}S$ $J = 3 - 2$ red	0.073 ± 0.011	
$C^{32}S$ $J = 3 - 2$ blue-wing	0.009 ± 0.002	
$C^{32}S$ $J = 3 - 2$ / $C^{32}S$ $J = 2 - 1$ intensity ratio [c]		
blueshifted emission	1.9 ± 0.5	2.7 ± 0.8
redshifted emission	2.4 ± 0.7	3.4 ± 1.0

a. derived from a two dimentional Gaussian fit.

b. calculated from the integrated flux, assuming a fractional CS abundance of 4×10^{-9} (Menten *et al.*1987, Walker *et al.*1990) and a gas kinetic temperature of 40 K (Menten *et al.*1987) with LTE and optically thin conditions.

c. evaluated using maps each of which is convolved with beam of the same size, $6''$.

Table 3.3 Derived quantities of $C^{34}S$ emission

	source A	source B
flux density (Jy km s^{-1})[a]	3.3 ± 0.5	0.7 ± 0.1
$M(H_2)$ ($M_\odot$)[b]	0.23 ± 0.03	0.05 ± 0.01

a. To estimate the flux densities of the $C^{34}S$ emission associated with each source we divide the emission into two portions on each side of a line, whose position angle is 30°, drawn through a midpoint between sources A and B.

b. assuming a fractional $C^{32}S$ abundance of 4×10^{-9} (Menten *et al.* 1987; Walker *et al.* 1990), a terrestrial $^{32}S/^{34}S$ abundance of 22.5 and a gas kinetic temperature of 40 K (Menten *et al.* 1987) with optically thin LTE conditions.

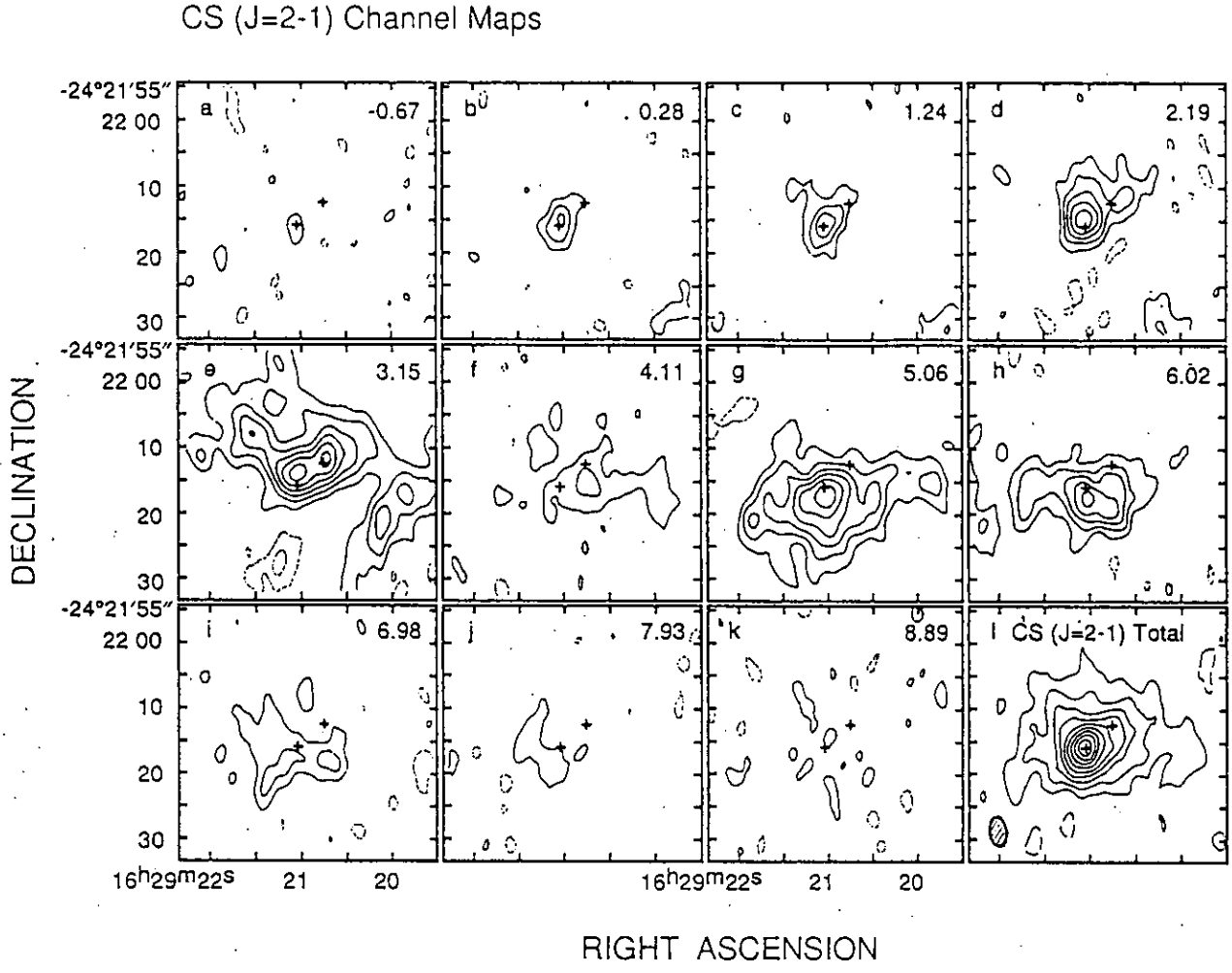

Figure 3.1. (a)-(k) Velocity channel maps of the $C^{32}S$ $J = 2 - 1$ emission with 0.96 km s^{-1} velocity width from V_{LSR} = -0.67 to 8.89 km s^{-1} . The center velocity of each channel is shown in each panel. Two crosses in each panel indicate the centimeter wavelength emission sources A and B (Wootten 1989). The contour interval is 3.05 K (2 σ). (l) Map of total $C^{32}S$ $J = 2 - 1$ intensity integrated over the velocity range from V_{LSR} = -0.67 to 7.93 km s^{-1} (Figs. 3.1 (a) - (j)). The contour interval is 10.4 K km s^{-1} (2 σ). The HPBW beam size is indicated by ellipse in the total intensity map.

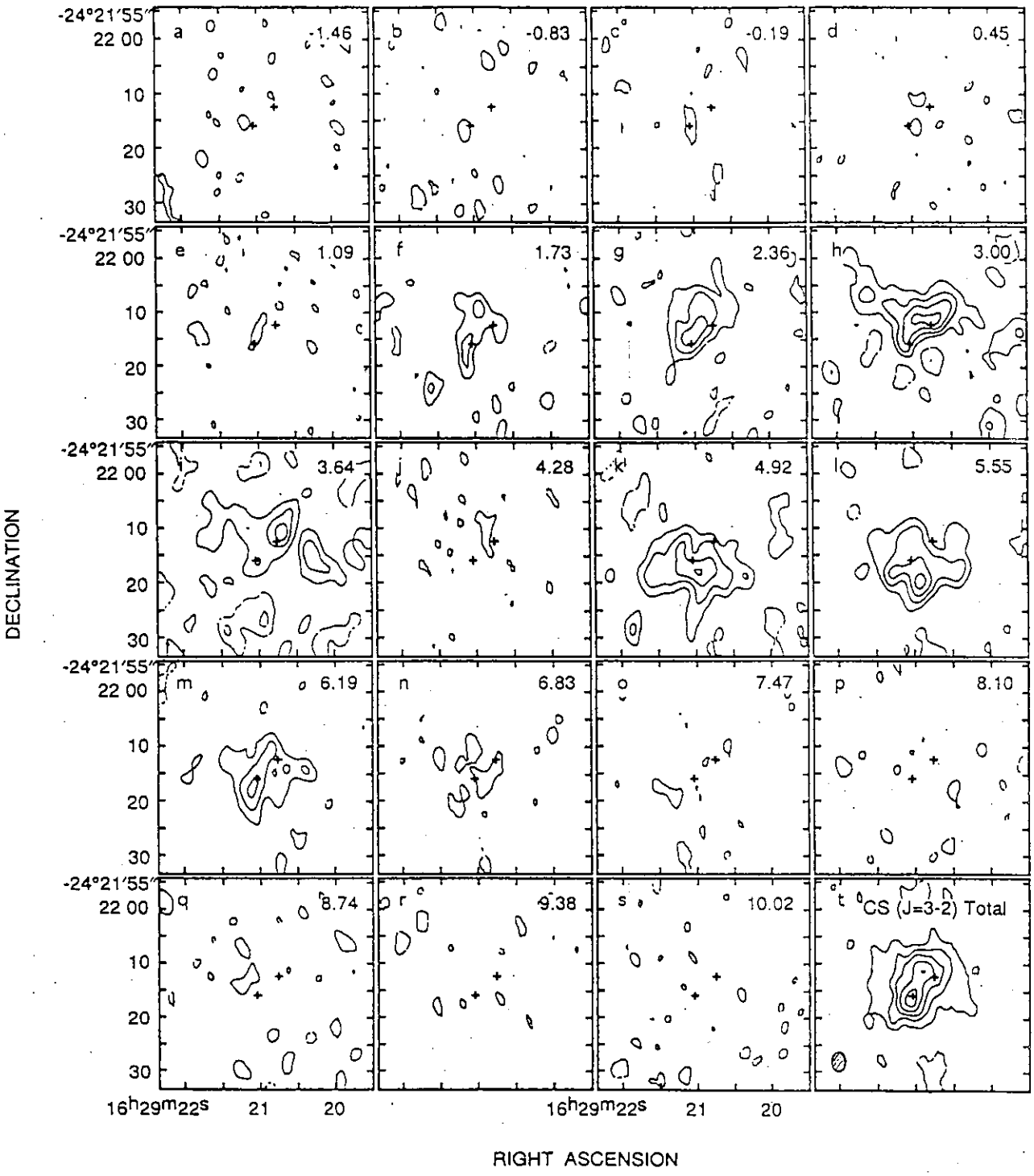

Figure 3.2. (a)-(s) Velocity channel maps of the $C^{32}S$ $J = 3 - 2$ emission with 0.64 km s^{-1} velocity width from V_{LSR} = -1.46 to 10.02 km s^{-1} . The contour interval is 5.30 K (2 σ). (t) Map of total $C^{32}S$ $J = 3 - 2$ intensity integrated over the velocity range from V_{LSR} = -1.46 to 6.83 km s^{-1} (Figs. 3.2 (a) - (n)). The contour interval is 24.3 K km s^{-1} (2 σ). The HPBW beam size is indicated by ellipse in the total intensity map.

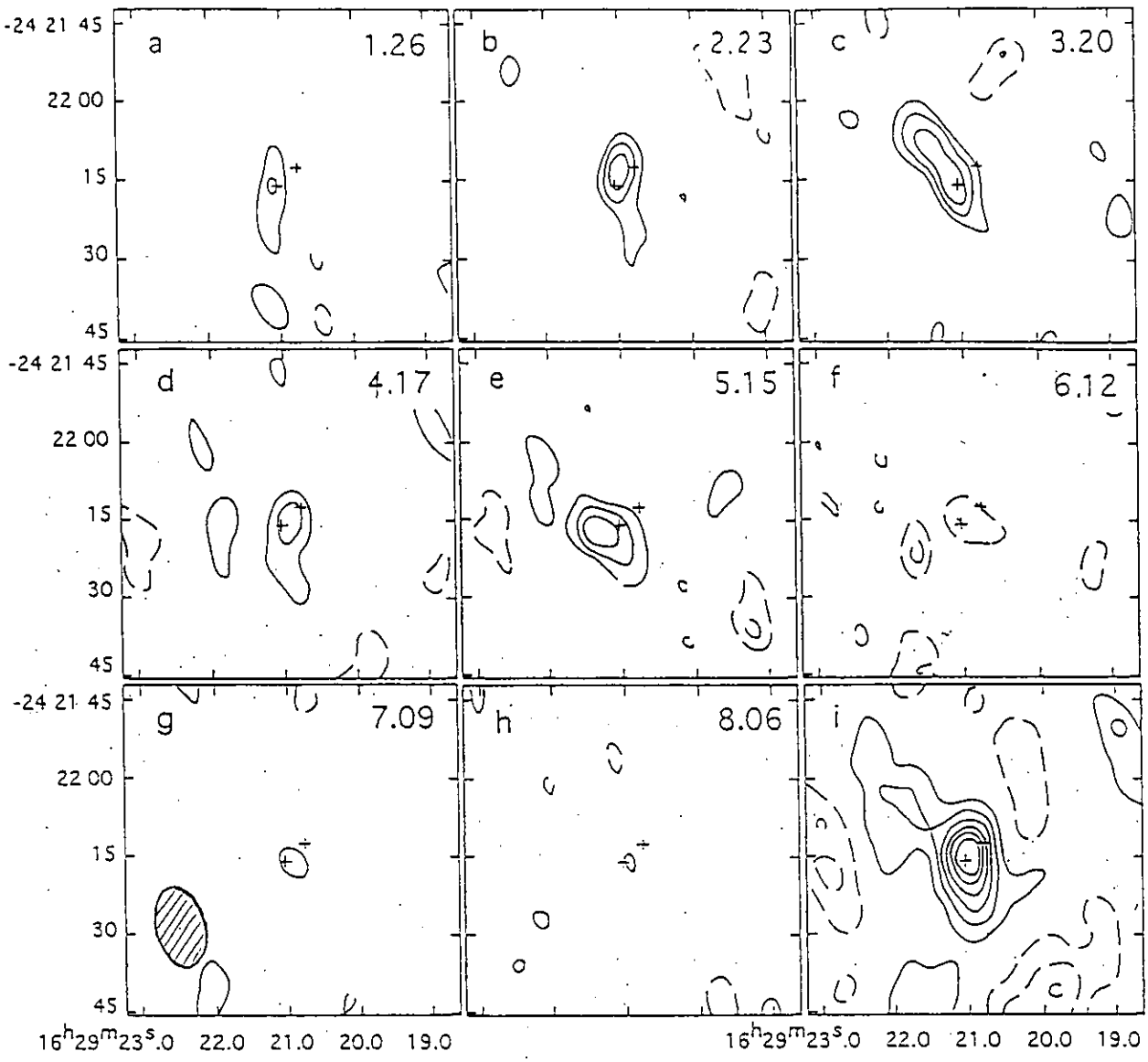

Figure 3.3. (a)-(h) Velocity channel maps of the $C^{34}S$ $J = 2 - 1$ emission with 0.97 km s^{-1} velocity resolution from V_{LSR} = 1.26 to 8.06 km s^{-1} . The center velocity of each channel is shown in each panel. Two crosses indicate the centimeter wavelength emission sources A and B (Wootten 1989). The contour starts from 0.32 K(2 σ) and the contour interval is 0.16 K (1 σ). The HPBW beam size is indicated by ellipse shown in the 7.09 km s^{-1} channel. (J) Map of total $C^{34}S$ $J = 2 - 1$ intensity integrated over the velocity range from V_{LSR} = 1.26 to 8.06 km s^{-1} (Figs. 3.3 (a) - (h)). The contour interval is 0.58 Kkm s^{-1} (1 σ).

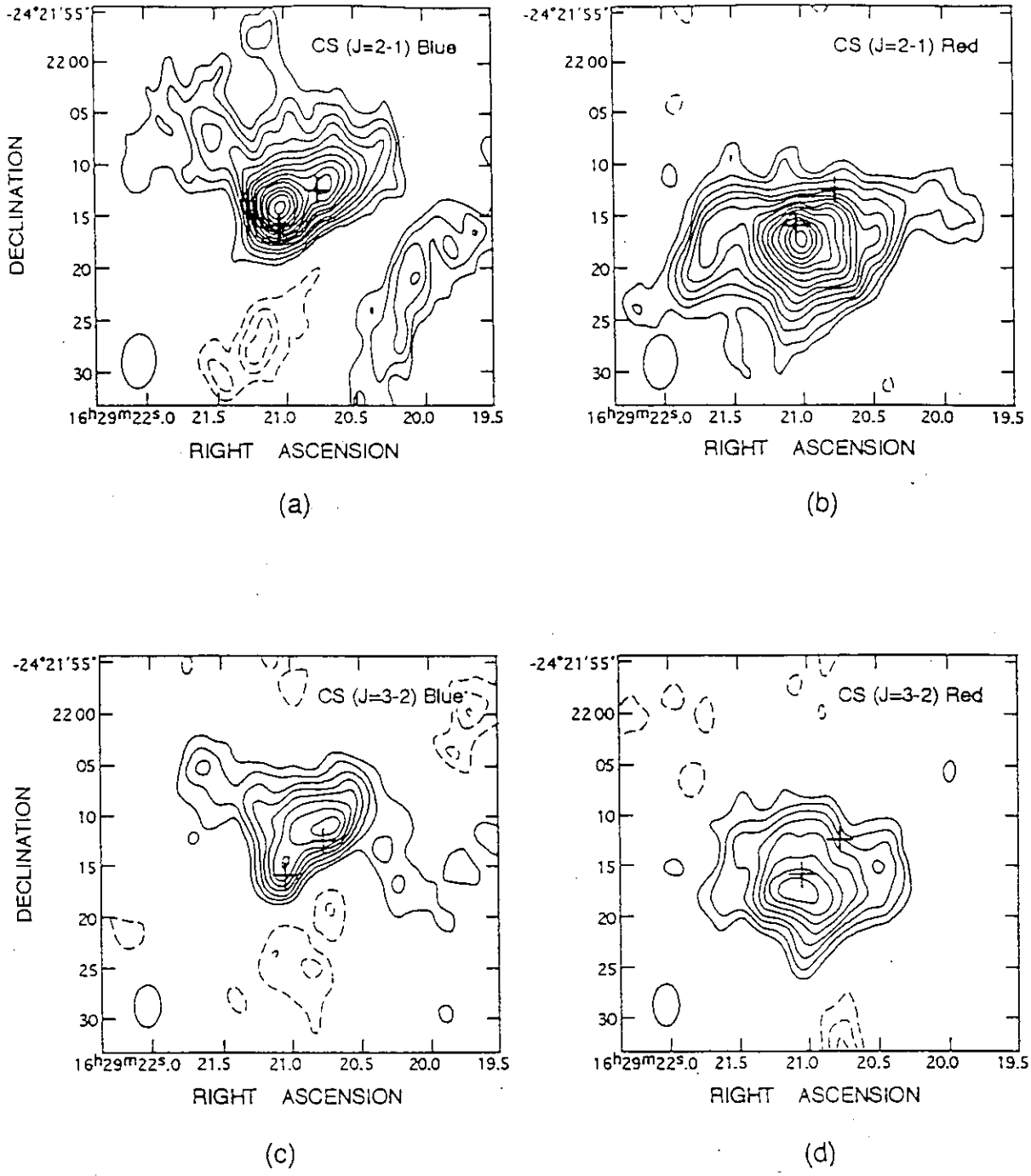

Figure 3.4. Maps of blue- and redshifted $C^{32}S$ emissions.

(a) The blueshifted $C^{32}S$ $J = 2 - 1$ component integrated over the velocity range from V_{LSR} = 2.19 to 3.15 km s^{-1} . (b) The redshifted $C^{32}S$ $J = 2 - 1$ component from V_{LSR} = 5.06 to 6.02 km s^{-1} . (c) The blueshifted $C^{32}S$ $J = 3 - 2$ component from V_{LSR} = 2.36 to 3.64 km s^{-1} . (d) The redshifted $C^{32}S$ $J = 3 - 2$ component from V_{LSR} = 4.92 to 6.19 km s^{-1} . In the $C^{32}S$ $J = 2 - 1$ maps the lowest contour is 2.84 K (2 σ) and the contour interval is 1.42 K (1 σ). In the $C^{32}S$ $J = 3 - 2$ maps the lowest contour is 11.2 K (2 σ) and the contour interval is 5.60 K (1 σ). The HPBW beam size is indicated by ellipse.

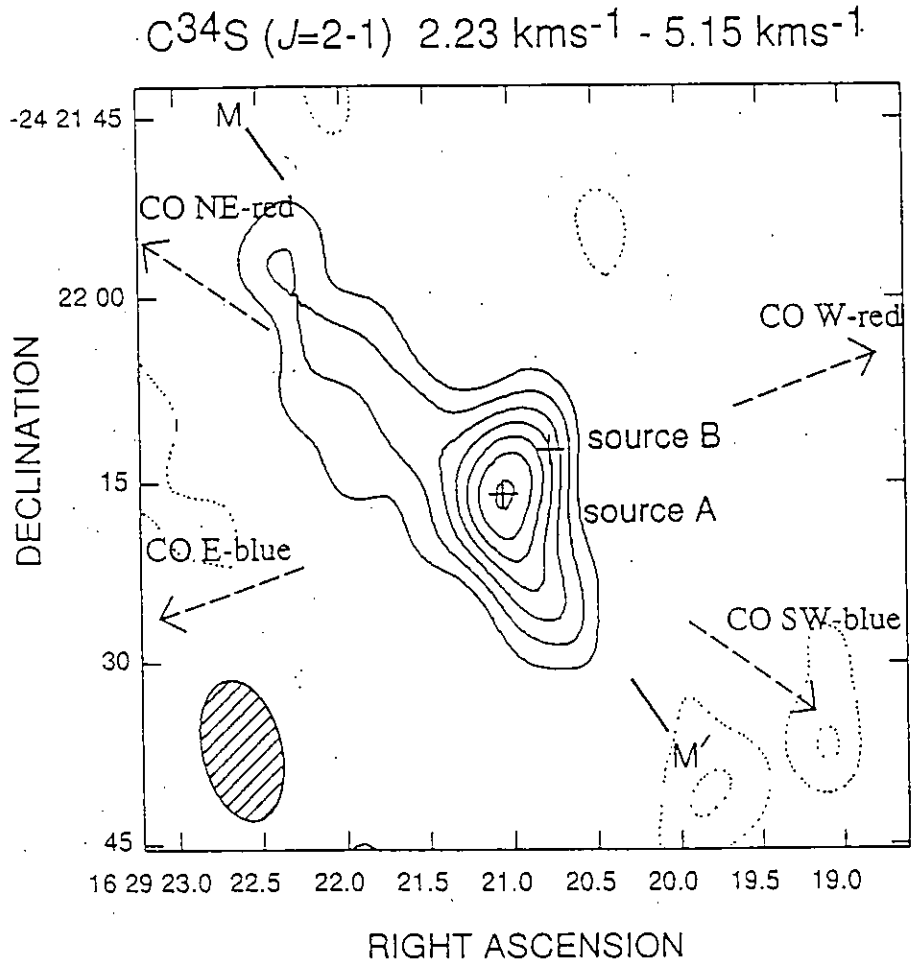

Figure 3.5. A map of $C^{34}S$ $J = 2 - 1$ emission integrated over the velocity range from V_{LSR} = 2.23 to 5.15 km s^{-1} . The lowest contour is 0.64 K (2 σ) and the contour interval is 0.32 K (1 σ). The directions of the four lobes of the high-velocity CO outflows are shown. The HPBW beam size is indicated by ellipse.

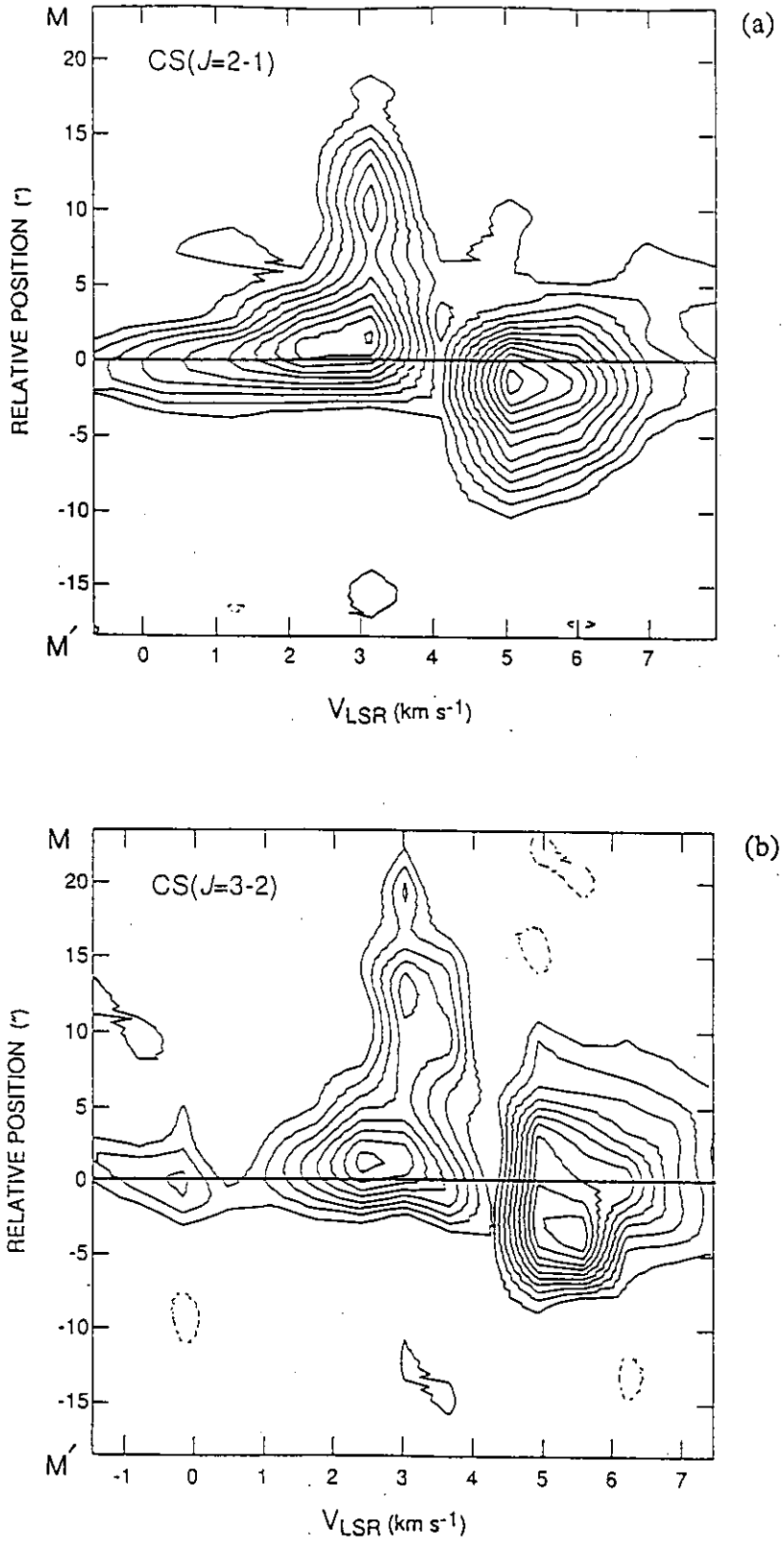

Figure 3.6. Position - velocity maps of (a) the $C^{32}S$ $J = 2 - 1$ and (b) the $C^{32}S$ $J = 3 - 2$ emission along the cut M-M' shown in Fig 3.5. The cutting line is the major axis of the disk-like structure through the position of source A. The contour interval is 1.53 K (1 σ) in the $C^{32}S$ $J = 2 - 1$ map and 1.64 K (1 σ) in the $C^{32}S$ $J = 3 - 2$. The solid line indicates the position of source A.

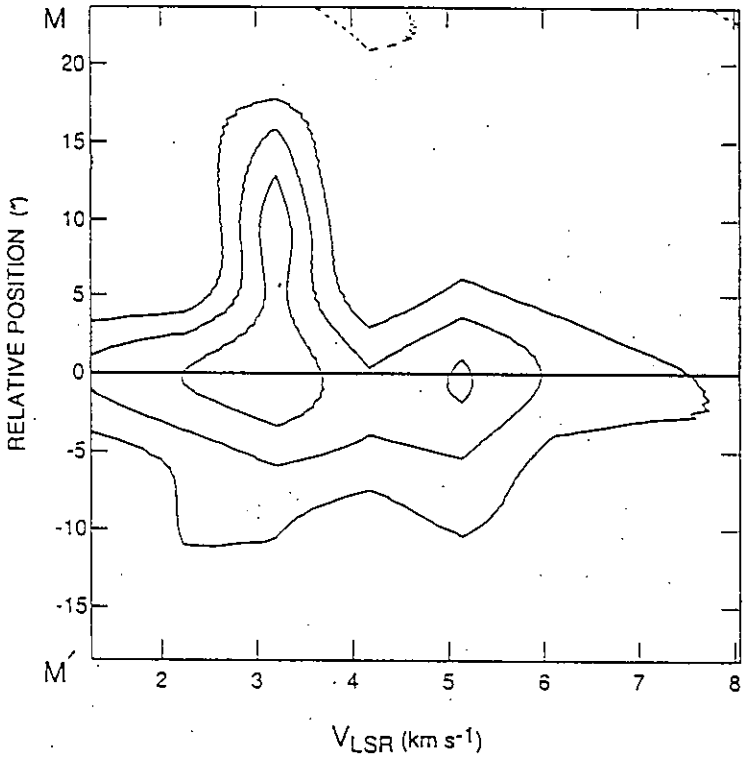

Figure 3.7. Position - velocity map of the $C^{34}S$ $J = 2 - 1$ emission along the cut M-M' shown in Fig 3.5. The contour interval is 0.16 K (1 σ). The solid line indicates the position of source A.

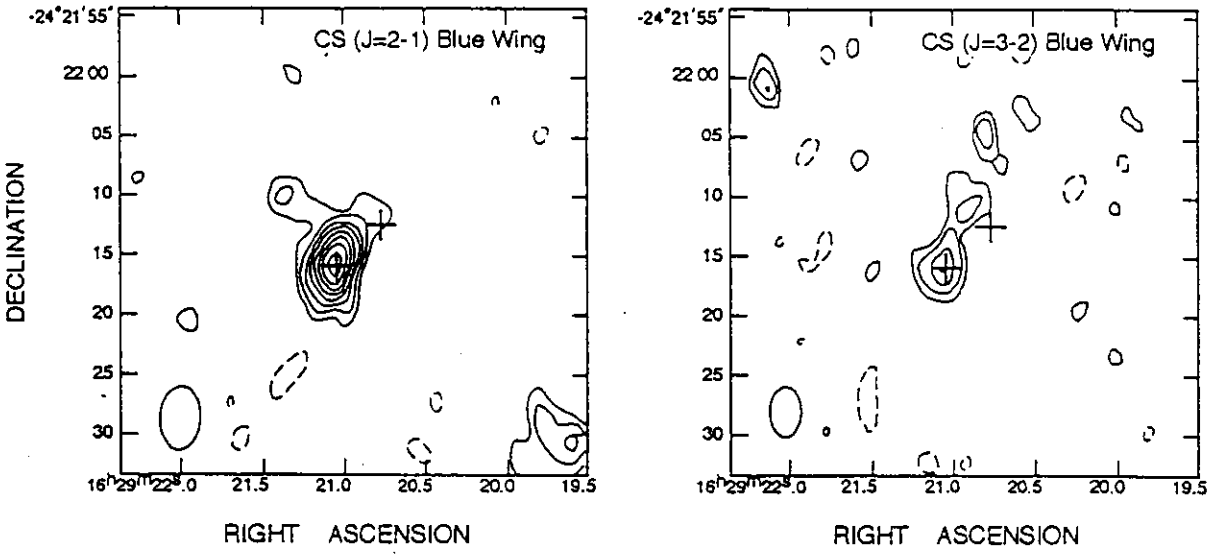

(a) (b)

Figure 3.8. Maps of $C^{32}S$ blueshifted wing component.

(a) The $C^{32}S$ $J = 2 - 1$ emission integrated over the velocity range from V_{LSR} = -0.67 to 1.24 km s^{-1} . (b) The $C^{32}S$ $J = 3 - 2$ emission from V_{LSR} = -1.46 to 1.09 km s^{-1} . In the $C^{32}S$ $J = 2 - 1$ map the lowest contour is 2.96 K (2 σ) and the contour interval is 1.48 K (1 σ). In the $C^{32}S$ $J = 3 - 2$ map the lowest contour is 11.1 K (2 σ) and the contour interval is 5.57 K (1 σ).

3.2 98 and 147 GHz continuum emissions

3.2.1 Maps of continuum emissions

i) Low-resolution maps of continuum emissions

In Figure 3.9 we show the maps of the continuum emission at 98 and 147 GHz, made using data from all configurations. Hereafter we call these maps low-resolution maps. Both the 98 and 147 GHz continuum emissions show similar spatial distribution and have two peaks which are spatially coincident with the peaks of the 2 cm continuum emission sources A and B, respectively (Wootten 1989). The spatial distribution and the total flux density of our 98 GHz continuum map agree with those of Walker *et al.* (1992) within the observational errors.

The 98 and 147 GHz continuum emissions have waists between two peaks. Therefore we divide the continuum emission into two portions on each side of the waist in order to derive the flux density associated with each of sources A and B by adding CLEAN components on each portion, assuming that the continuum emission on each side is associated with the corresponding radio source. The flux densities of the continuum emission associated with source A are 102 $\pm$ 15 mJy at 98 GHz and 352 $\pm$ 53 mJy at 147 GHz, while those associated with source B are 198 $\pm$ 30 mJy at 98 GHz and 720 $\pm$ 108 mJy at 147 GHz.

The beam deconvolved source sizes of the 98 GHz continuum emission, which are estimated from two dimensional Gaussian fit to the peaks is $5''.6 \times 3''.1$ (P.A. = 156°) for source A and $3''.5 \times 1''.8$ (P.A. = 16°) for source B. The continuum emission associated with source A is marginally resolved while that associated with source B is not resolved with our beam size of $5''.2 \times 3''.1$. The 147 GHz continuum map shows another weak component about $3''.8$ east of source B, which is unrecognizable in the 98 GHz continuum map. The slight difference of the spatial distributions between the two maps may be due to errors of the 147 GHz observations, for example an atmospheric effect. Therefore it is difficult to fit the 147 GHz continuum emission with Gaussian.

ii) High-resolution maps of continuum emissions

In Figure 3.10 we show the maps of the continuum emission at 98 and 147 GHz, made using data from the most sparse configuration. The beam size is 2″.7 × 1″.7 (PA = -12°) for the 98 GHz and 2″.0 × 1″.1 (PA = -2°.4) for the 147 GHz. Hereafter we call these maps high-resolution maps. Both the 98 and 147 GHz continuum emissions consist of two compact cores and each of the compact cores is associated with each of the 2 cm continuum sources A and B (Wootten 1989). The flux densities of the continuum emission associated with source A are 55 ± 8.3 mJy at 98 GHz and 140 ± 21 mJy at 147 GHz, while those associated with source B are 120 ± 18 mJy at 98 GHz and 260 ± 39 mJy at 147 GHz.

3.2.2 Flux densities and emissivity indices

i) Estimation of free-free contribution

To examine the contribution of the free-free emission we must know the origin of the centimeter emission. Figure 3.11 shows the millimeter to centimeter spectra of both sources A and B. The spectral index of the centimeter emission is 0.4 ± 0.1 for source A, which indicates the centimeter emission to be the free-free emission, while 2.1 ± 0.4 for source B, which implies that the centimeter emission mainly originates from the dust (Mundy *et al.* 1992). The contribution of the free-free emission for source A is estimated to be 10 mJy at 98 GHz and 13 mJy at 147 GHz from the extrapolation of the centimeter radio spectrum (Mundy *et al.* 1992), and those are less than 10 % of the millimeter fluxes. Since there seems to be little contribution from the free-free emission from source B, the millimeter emissions associated with source B arise from dust grains.

ii) High-resolution maps - emissions from circumstellar dust disks

In the high-resolution maps the flux densities of the dust emission, *i.e.*, the continuum emission from which the free-free component are subtracted, associated with source A are 45 ± 8.3 mJy at 98 GHz and 128 ± 21 mJy at 147 GHz. The spectral index α ($F_\nu \propto \nu^\alpha$)

is estimated to be 2.46 ± 0.67 for source A and 1.81 ± 0.56 for source B, using the flux densities of 98 and 147 GHz. If the emission is optically thin and the temperature is high enough to make the Rayleigh-Jeans approximation valid ($T > h\nu/k \sim 4.8$ K at 98 GHz and 7.2 K at 147 GHz), then dust emissivity index β is estimated using the relation of β= α−2. The dust emission is likely to be optically thin at millimeter wavelength, and the dust temperature of IRAS 16293-2422, ~ 40 K, is high enough that we can estimate β index from the spectral index. The β index is estimated to be 0.46 ± 0.67 for source A and -0.19 ± 0.56 for source B. The β indices of unity or smaller is reported in compact circumstellar disk around pre-main-sequence stars (Beckwith and Sargent 1991). Thus the facts that the distributions of the dust emissions are compact and the emissivity indices are close to zero suggest that the compact dust emissions arise from circumstellar dust disk around each star.

iii) Low-resolution maps - emission from dust envelopes and disks

In the low-resolution maps the flux densities of the dust emission associated with source A are 92 ± 15 mJy at 98 GHz and 340 ± 53 mJy at 147 GHz, respectively. The spectral index is estimated to be 3.1 ± 0.60 for source A and 3.0 ± 0.56 for source B. These values corresponds to dust emissivity index β of 1.1 ± 0.60 for source A and 1.0 ± 0.56 for source B, which are consistent with that obtained by single dish observations (Walker *et al.* 1990).

It is clear that there exists each extended dust envelope around each of source A and B, because each total flux of sources A and B, obtained from the lower resolution maps at 98 and 147 GHz, is much higher than that obtained from the high-resolution map (the total flux is roughly proportional to the beam size of the observations, if we make maps with different beam sizes and obtain the flux density for each; Figure 3.12). Hence the dust emissions around each source shown in the low-resolution maps are composed of two components, *e.g.*, extended component (dust envelope) and compact component (dust disk).

iv) emission from dust envelopes

The dust flux densities of the extended components (dust envelopes), estimated from the flux densities of the low- and high-resolution maps, associated with source A are 47 ± 8.7 mJy at 98 GHz and 210 ± 34 mJy at 147 GHz, and those associated with source B are 78 ± 12 mJy at 98 GHz and 460 ± 69 mJy at 147 GHz. The spectral index is estimated to be 3.5 ± 0.7 for source A and 4.2 ± 0.6 for source B. These values correspond to dust emissivity index β of 1.5 ± 0.7 for source A and 2.2 ± 0.6 for source B, which are roughly equal to the interstellar value.

3.2.3 Mass estimation from the dust emissions

i) Formulae and assumptions

Thermal emission from dust grains is highly useful to estimate amount of dust grains. The total flux density of the dust emission associated with source B are higher than that associated with source A at both 98 GHz and 147 GHz. This suggests that the dust mass around source B is higher than that around source A. From the flux density of the dust emission the gas mass can be estimated using the following equation.

From the total flux densities of the 98 GHz continuum emission, we have

$$M = 3.4 \times 10^{-6}[\exp(4.7/T_d) - 1]\left(\frac{D}{\mathrm{pc}}\right)^2\left(\frac{\mathrm{C_\nu}}{\mathrm{gcm^{-2}}}\right)\left(\frac{F_\nu}{\mathrm{Jy}}\right) M_\odot, \quad (4)$$

and from the total flux densities of the 147 GHz continuum emission, we have

$$M = 9.6 \times 10^{-7}[\exp(7.2/T_d) - 1]\left(\frac{D}{\mathrm{pc}}\right)^2\left(\frac{\mathrm{C_\nu}}{\mathrm{gcm^{-2}}}\right)\left(\frac{F_\nu}{\mathrm{Jy}}\right) M_\odot, \quad (5)$$

where T_d is the dust temperature, D is the distance to the continuum source, and $\mathrm{C_\nu}$ is the conversion coefficient from continuum flux density, F_ν, to H_2 column density and is given as (Hildebrand 1983),

$$\mathrm{C_\nu} = 27 \times \left(\frac{\lambda/0.4}{\mathrm{mm}}\right)^\beta \ \mathrm{g\ cm^{-2}}. \quad (6)$$

In order to estimate the gas mass, we have to know the information about the β index and the dust temperature. The β indices are calculated in earlier section, and are nearly equal

for sources A and B within the observational errors. Thus we assume $\beta = 0$ for the compact dust disks and $\beta = 1.5$ for the dust envelopes. The dust temperature is deduced to be 32 - 45 K from a model fit to the spectral energy distribution (Wootten 1989, Walker *et al.* 1990, Mezger *et al.* 1990). Here we adopt 40 K as the dust temperature.

ii) Estimation of gas masses from the dust emissions

For the compact dust disks we estimate the gas mass to be 0.013 $\pm$ 0.002 $M_\odot$ from 98 GHz and 0.016 $\pm$ 0.003 $M_\odot$ from 147 GHz for source A, while 0.033 $\pm$ 0.005 $M_\odot$ from 98 GHz and 0.034 $\pm$ 0.005 $M_\odot$ from 147 GHz for source B. The estimated gas masses are listed in Table 3.4.

For the extended dust envelopes we estimate gas the gas mass to be 0.29 $\pm$ 0.05 $M_\odot$ from 98 GHz and 0.31 $\pm$ 0.05 $M_\odot$ from 147 GHz for source A, while 0.46 $\pm$ 0.07 $M_\odot$ from 98 GHz and 0.67 $\pm$ 0.10 $M_\odot$ from 147 GHz for source B. The estimated gas masses are listed in Table 3.5.

iii) Effects of β index on mass estimation

To ascertain uncertainties involved in β index, we estimate the gas mass using β index derived from the flux densities of 98 GHz and 147 GHz and assuming the dust temperature of 40 K. For the compact dust disks we estimate the gas mass to be 0.034 $\pm$ 0.005 $M_\odot$ from 98 GHz and 0.035 $\pm$ 0.005 $M_\odot$ from 147 GHz for source A, while 0.024 $\pm$ 0.004 $M_\odot$ from 98 GHz and 0.025 $\pm$ 0.004 $M_\odot$ from 147 GHz for source B. For the extended dust envelopes we estimate the gas mass to be 0.29 $\pm$ 0.05 $M_\odot$ from 98 GHz and 0.31 $\pm$ 0.05 $M_\odot$ from 147 GHz for source A, while 1.9 $\pm$ 0.29 $M_\odot$ from 98 GHz and 2.1 $\pm$ 0.32 $M_\odot$ from 147 GHz for source B. The derived gas mass of the dust envelope around source B is significantly larger than the mass derived from CS fluxes ($\simeq$ 0.05 $M_\odot$). Thus the assumed dust temperature is suspected to be low for source B.

iv) Comparison of the masses estimated from the dust emissions with that from the CS emissions

The gas masses of the dust envelope, 0.3 $M_{\odot}$ and 0.5 $M_{\odot}$for sources A and B, respectively, are larger than those estimated from the $C^{34}S$ emission, 0.23 $M_{\odot}$ and 0.05 $M_{\odot}$ for the disk-like structure around source A and the compact gas around source B, respectively. Even if we consider the uncertainty of the β index and the dust temperature involved in the estimation of the gas mass from the dust emission, there is discrepancy between the masses from the $C^{34}S$ emissions and those from the dust emissions. One possibility is that the $C^{34}S$ $J = 2 - 1$ emission become optically thick in the very vicinity of the central stars traced by the dust emission.

Table 3.4 Derived quantities of compact dust disks

	souce A	source B
98GHz integrated flux (mJy)	45 ± 8.3 [a]	120 ± 18
150GHz integrated flux (mJy)	128 ± 21 [a]	260 ± 39
α	2.46 ± 0.67	1.81 ± 0.56
β[b]	0.46 ± 0.67	-0.19 ± 0.56
$M_{gas}(\beta=0,40K^c)^d$ from 98GHz flux ($M_\odot$)	0.013 ± 0.002	0.033 ± 0.005
$M_{gas}(\beta=0,40K^c)^d$ from 150GHz flux ($M_\odot$)	0.016 ± 0.003	0.034 ± 0.005
$M_{gas}(\beta,40K)^e$ from 98GHz flux ($M_\odot$)	0.034 ± 0.005	0.024 ± 0.004
$M_{gas}(\beta,40K)^e$ from 150GHz flux ($M_\odot$)	0.035 ± 0.005	0.025 ± 0.004

a. the flux after subtraction of the contribution of the free-free emission

b. $\kappa_\nu \propto \nu^\beta$ ($\beta = \alpha$-2)

c. from a model fit to the spectral energy distribution (Wootten 1989)

d. gas masses estimated assuming $\beta = 0$ and $T_d = 40$ K

e. gas masses estimated using β derived in this work and assuming $T_d = 40$ K

Table 3.5 Derived quantities of dust envelopes

	souce A	source B
98GHz integrated flux (mJy)	47 ± 8.7 [a]	78 ± 12
150GHz integrated flux (mJy)	210 ± 34 [a]	460 ± 69
α	3.5 ± 0.7	4.2 ± 0.6
β[b]	1.5 ± 0.7	2.2 ± 0.6
M_{gas}(β=1.5,40K[c])[d] from 98GHz flux ($M_\odot$)	0.29 ± 0.05	0.46 ± 0.07
M_{gas}(β=1.5,40K[c])[d] from 150GHz flux ($M_\odot$)	0.31 ± 0.05	0.67 ± 0.10
M_{gas}(β,40K)[e] from 98GHz flux ($M_\odot$)	0.29 ± 0.05	1.9 ± 0.29
M_{gas}(β,40K)[e] from 150GHz flux ($M_\odot$)	0.31 ± 0.05	2.1 ± 0.32

a. the flux after subtraction of the contribution of the free-free emission

b. $\kappa_\nu \propto \nu^\beta$ ($\beta = \alpha$-2)

c. from a model fit to the spectral energy distribution (Wootten 1989)

d. gas masses estimated assuming β = 1.5 and T_d = 40 K

e. gas masses estimated using β derived in this work and assuming T_d = 40 K

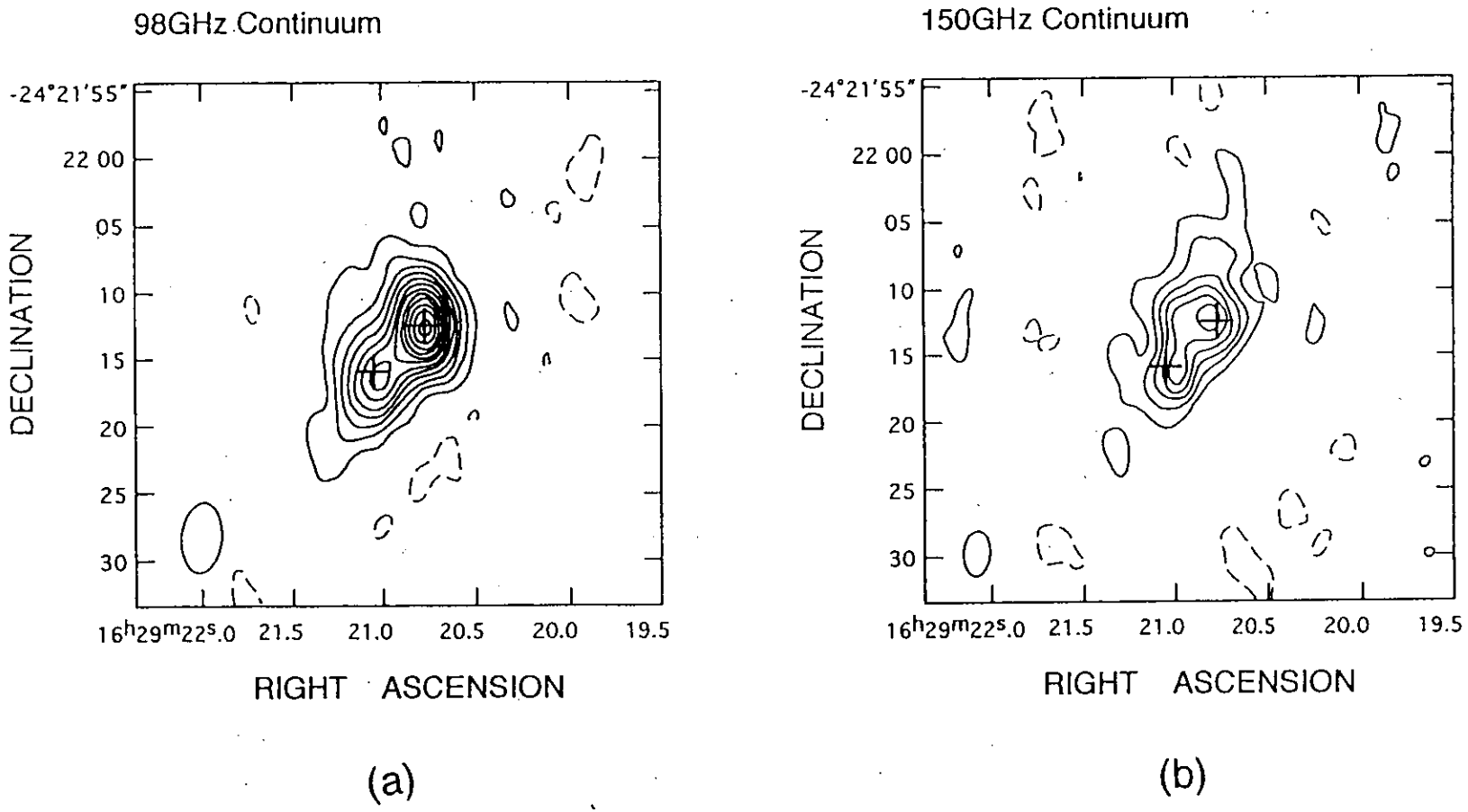

Figure 3.9. Low resolution maps of (a) 98 GHz and (b) 150 GHz continuum emission. The contour interval is 13.2 mJy beam^{-1}(2 σ) in the 98 GHz map and 40.8 mJy beam^{-1}(2 σ) in the 150 GHz map. Two crosses in each panel indicate the centimeter wavelength emission sources A and B (Wootten 1989). The HPBW beam size is indicated by ellipse.

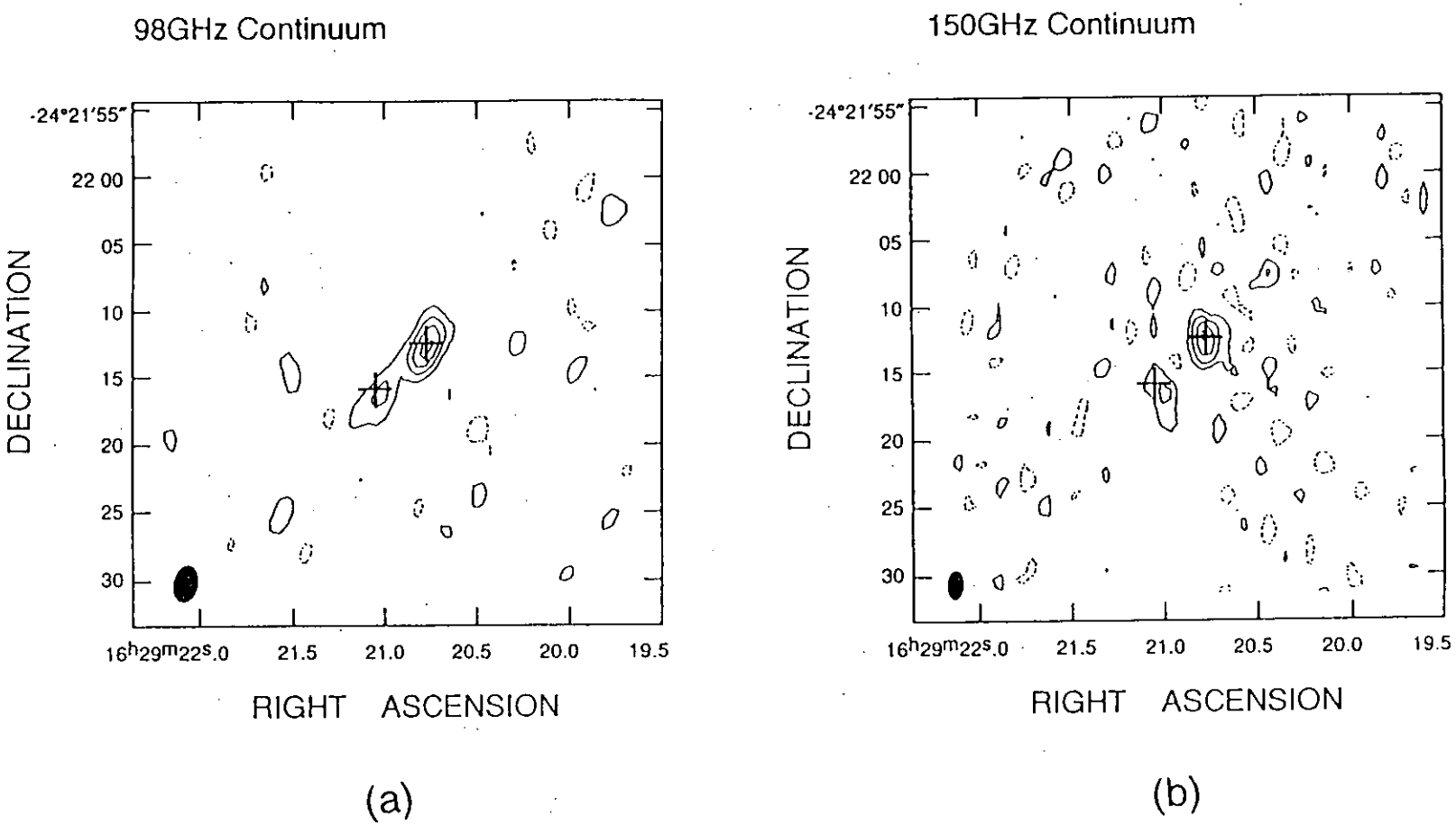

Figure 3.10. High resolution maps of (a) 98 GHz and (b) 150 GHz continuum emission. The contour interval is 22.2 mJy beam^{-1}(2 σ) in the 98 GHz map and 49.2 mJy beam^{-1}(2 σ) in the 150 GHz map. The HPBW beam size is indicated by ellipse.

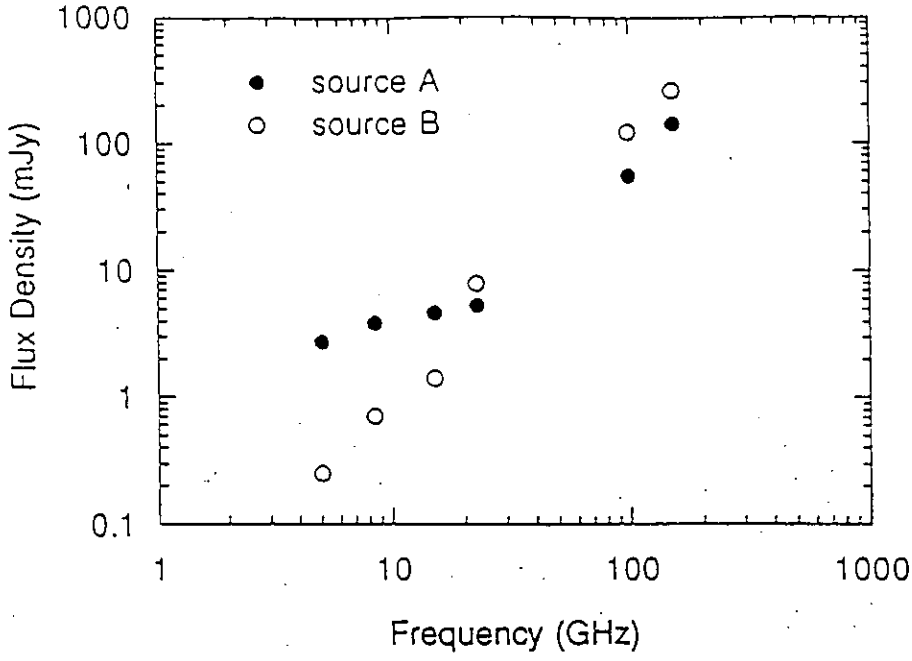

Figure 3.11. Spectrum of sources A and B between 5 GHz and 150 GHz. The 5, 8.4, 15, and 22.5 GHz data are from Mundy *et al.* (1992) and the 98 and 150 GHz data are from this work.

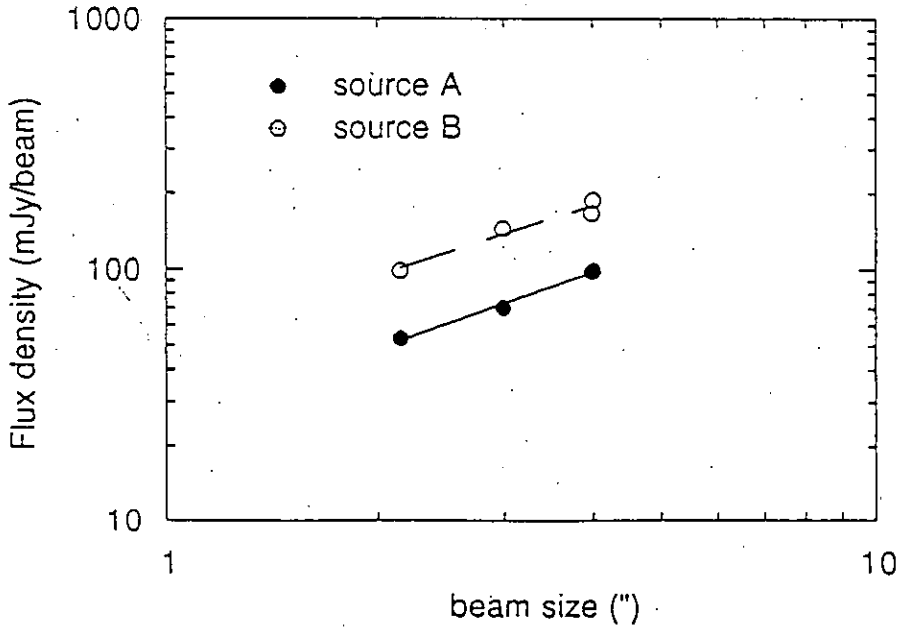

Figure 3.12. Plot of flux density of the dust emission against various beam size. All data are from this work.

4 Gas and dust environments around sources A and B

Before going to detailed discussion, we summarize the gas and dust environments around sources A and B based on our observational results; we present the summary of molecular gas features (sec. 4.1), physical nature of molecular gas (sec. 4.2), summary of dust environments (sec.4.3), and physical nature of dust features (sec. 4.4) .

4.1 Summary of Molecular Gas Features

i) Gas disk around source A

Disk-like structure of molecular gas just centered at source A was found in the $C^{34}S$ $J = 2-1$ maps (Figure 3.5). The corresponding part of the feature is also seen in both the $C^{32}S$ $J = 3-2$ and $C^{32}S$ $J = 2-1$ maps (Figure 3.4), though the elongated structure are not so clear compared with that in the $C^{34}S$ $J = 2-1$ maps because of contaminations of the other features. The velocity structures of $C^{32}S$ $J = 3-2$ and $C^{32}S$ $J = 2-1$ maps show that the kinematical center of the molecular gas is also centered at source A and the molecular gas is rotating around source A. These facts suggest that there exists a rotating disk of molecular gas around source A.

ii) Low velocity EW "streamer" (V_{LSR} = 5 km s^{-1}) around source A

EW elongation of molecular gas was found in both the $C^{32}S$ $J = 3-2$ and $C^{32}S$ $J = 2-1$ maps at V_{LSR} = 5 km s^{-1} and seems to be associated with source A. This direction of the elongation is apparently coincident with the direction of more prominent one of the two outflows (PA=110°), but the relative velocity of the molecular gas to the systemic velocity is as small as 1 km s^{-1} . Then, this molecular gas would not be a part of the molecular outflow but possibly the ambient molecular gas compressed and accelerated by the interaction with the outflow. Hereafter, we call this feature a low velocity EW "streamer".

iii) Compact blue-wing emission centered at source A

It was found that there exists a compact blue-wing emission centered at source A. This emission was seen in both the $C^{32}S$ $J = 3 - 2$ and the $C^{32}S$ $J = 2 - 1$ maps and the distribution was not sufficiently resolved with our beams ($4''.2 \times 2''.6$). The velocity range of the emission is V_{LSR} = -1 km s^{-1} to 1 km s^{-1}. There is no wing emission around source B.

iv) Molecular gas associated with source B

Molecular gas was found to exist closely associated with source B at around V_{LSR} = 3.1 km s^{-1} (only two of the channel maps) in both the $C^{32}S$ $J = 3 - 2$ and $C^{32}S$ $J = 2 - 1$ maps. However, no emission associated with source B was seen in $C^{34}S$ $J = 2 - 1$ maps, and except for the above-mentioned channel, there is no $C^{32}S$ $J = 3 - 2$ and $C^{32}S$ $J = 2 - 1$ emission just centered at source B.

4.2 Physical Nature of Molecular Gas

i) Gas disk around source A

The estimated gas mass is 0.23 $M_{\odot}$ from the map of $C^{34}S$ $J = 2 - 1$. The radius and the rotational velocity at this radius are estimated to be 420 AU and 1 km s^{-1}, respectively, by using the two redshifted and blueshifted peaks in the P-V diagrams in $C^{32}S$ $J = 2 - 1$ and $C^{32}S$ $J = 3 - 2$ (Figure 3.6). The systemic velocity is about 4 km s^{-1}. The position angle of the disk major axis is 30°, and the disk is roughly perpendicular to the direction of the more prominent one of the two pairs of the outflows (PA=110°). The gas disk rotates around source A, roughly in the same sense as the rotation of the parent molecular cloud core (Menten *et al.* 1987). We discuss about the kinematics of the disk in sec. 5.1.

ii) Low velocity EW "streamer" (V_{LSR} = 5 km s^{-1}) around source A

The estimated gas mass is 0.024 $M_{\odot}$, the length is as long as 4600 AU (probably extending outside the F.O.V of the observations). The position angle of the elongation is about 100-110°, just being coincident with that of the more prominent one of the outflows. It is, therefore, very likely that this feature is associated with the more prominent outflow.

iii) Compact blue-wing component centered at source A

The H_2 mass is 0.01 $M_\odot$, and the size is smaller than 4″in radius. The velocity relative to V_{sys} is as large as 4-6 km s^{-1} . It should be noted that the wing emission is seen only at the blue-shifted side and there is no clear sign of corresponding red-shifted emission.

iv) Molecular gas associated with source B

The H_2 mass is 0.05 $M_\odot$. This H_2 mass is rather smaller than that of the disk around source A. The velocity (relative to V_{sys}) is -1 km s^{-1} and the velocity width is roughly estimated to be 2 km s^{-1} from the channel maps of $C^{32}S$ $J = 2 - 1$ and $C^{32}S$ $J = 3 - 2$. The molecular gas seems to be slightly extended but be as small as 6-8″in diameter.

4.3 Summary of Dust Environments

i) Compact dust cores around sources A and B

It was revealed from our high-resolution maps at 98 and 147 GHz (beam at 147 GHz is 2.0″$\times$ 1.1″corresponding a beam radius of 160 AU $\times$ 90 AU) that there exist very compact cores just associated with both sources A and B. The spectral indices of the cores are estimated to be 2.5 $\pm$ 0.7 and 1.8 $\pm$ 0.6 for sources A and B, respectively, suggesting that the compact cores have a nature different from that of the extended dust envelope with a spectral index of $\sim$ 3. These observational results (compact distribution and relatively flatter spectrum) suggest that each compact dust core is a dust disk surrounding each central protostar. Hereafter, we call the compact core a compact dust disk.

The flux densities of the compact dust disk in source B obtained with the millimeter observations and those at centimeters of source B obtained with VLA can be connected by a single power law with a spectral index of $\sim$ 2 (Figure 3.11).

ii) Dust envelopes around sources A and B

It is clear that an extended dust envelope exists around each of source A and B, because each

total flux of sources A and B, obtained from the lower resolution maps at 98 and 147 GHz, is much higher than that obtained from the high-resolution map (the total flux is roughly proportional to the beam size of the observations, if we make maps with different beam sizes and obtain the flux for each, see Figure3.12). This is supported by the fact that the beam-deconvolved size of the each dust component is estimated to be 3″- 4″. Because the disk of the molecular gas around source A has a larger size, the dust envelope would be the central part of the disk structure.

The spectral index is roughly estimated to be 3 using the total fluxes at 98 GHz and 147 GHz (including sources A and B), and this corresponds to dust emissivity index of 1, which is very consistent with that obtained by single dish observations. For the extended components, the spectral indices are estimated to be 3.5 $\pm$ 0.7 and 4.2 $\pm$ 0.6 for sources A and B, respectively. The extended components have much steeper spectral indexes than the compact dust disk components.

4.4 Physical Nature of Dust Components

i) Compact disks

The gas mass of the compact disk in source A is estimated to be 0.01 $M_{\odot}$ by assuming $\beta = 0$ and by using the flux densities at 98 and 147 GHz, subtracted with free-free components. H_2 mass of the compact disk around source B is also obtained to be 0.03 $M_{\odot}$ assuming $\beta = 0$.

ii) Dust envelopes

The H_2 mass of dust envelopes around sources A and B was estimated to be 0.3 and 0.6 $M_{\odot}$ by assuming β=1.5 for both the dust envelopes. Although the sizes of the envelopes are rather uncertain, they are roughly 3″-5″in diameter.

5. Kinematical structure of molecular gas around source A : the disk and the blue wing

5.1 Kinematics and stability of the disk

The infalling motion is claimed to exist in the molecular gas envelope in IRAS16293-2422, from the analysis of the spectral line formation solving the radiative transfer models of collapsing cloud with rotation (Zhou 1995, Walker *et al.* 1986). Then, it is very interesting to investigate the kinematics of the molecular gas disk around source A and also the dynamical instability of the disk.

5.1.1 Kinematics of the disk : rotationally supported or infalling ?

Firstly, we compare the observed rotation velocity with the Keplerian velocity expected from the central mass associated with source A. If the disk is not rotationally supported and the rotation velocity is smaller than the Keplerian velocity, the disk is possibly a part of the infalling envelope with a flattened shape. The rotational velocity is estimated to be about 1 km s^{-1} /sin i at r= 420 AU if we use two redshifted and blueshifted peaks in the P-V diagrams in $C^{32}S$ $J = 2 - 1$ and $C^{32}S$ $J = 3 - 2$ (Figure 3.6). Prior to the estimation of the Keplerian velocity, we roughly derive the stellar mass of source A. If the age of the star is almost the same as that of the bipolar outflows, 1.4×10^4 years (Mizuno *et al.* 1990), and if the mass accretion rate onto the star is constant throughout the evolution of the protostar and actually, 1.3×10^{-5} $M_{\odot}yr^{-1}$ in the case of the gas temperature of 40 K, the mass is calculated to be 0.2 $M_{\odot}$. This mass is likely a lower limit to the stellar mass, because the stellar age is actually older than that of the bipolar outflow. There is another way to estimate the stellar mass by using the bolometric luminosity of IRAS 16293-2422. If we assume the bolometric luminosity is almost the same as the accretion luminosity, the stellar mass is derived to be 0.45 $M_{\odot}$ by using the following equation.

$$L_{acc} = \frac{GM_{*}\dot{M}}{R_{*}}, \tag{7}$$

where $\dot{M}$ is mass accretion rate onto the star, which is $\sim 1.3 \times 10^{-5}$ $M_{\odot}\mathrm{yr}^{-1}$ in the case of the gas temperature of 40 K, and R_* is the radius of the protostar, which is 4 $R_{\odot}$(Adams and Shu 1985). The derived mass is an upper limit to the stellar mass, if we consider the bolometric luminosity contributed from source B.

The Keplerian velocity is about 1.3- 1.5 km s^{-1} at r=400 AU assuming that the mass inside r= 400 AU is 0.7- 1 $M_{\odot}$, which is estimated by summing up the masses of the compact dust envelope (0.3 $M_{\odot}$), the disk (0.23 $M_{\odot}$), and the derived stellar mass (0.2- 0.5 $M_{\odot}$). The rotation velocity seems to be roughly consistent with or slightly smaller that the estimated Keplerian velocity, if the disk is nearly edge-on (*i.e.*, sin i = 1). The calculated Keplerian rotation curves for 0.5, 1, 1.5, and 2 $M_{\odot}$ are plotted on the P-V diagrams as shown in Figures 5.1. The northern parts of the P-V diagrams seem to be well traced by the Keplerian disk model with a mass of about 1 $M_{\odot}$, although there is no clear counterpart at the southern part. It should be noted that it is currently unclear whether the disk is rotationally supported or not because of large uncertainties in the rotation velocity and the stellar mass. The future observations with higher angular resolution and higher velocity resolution is required to discriminate two possibilities, a Keplerian disk or an infalling envelope.

5.1.2 Stability of the disk

If the mass of the rotating disk is higher than about 0.3 $\times$ M_*, Toomre's Q parameter for the disk is smaller than 1, the disk is unstable against gravitational instability (Shu *et al.* 1990). In the case of the disk around source A, the disk mass of 0.53 $M_{\odot}$(compact dust envelope + disk) is comparable to or higher than the stellar mass (0.2- 0.5 $M_{\odot}$). This fact would not change, even if we consider the uncertainties in the estimated masses. This means that the disk is actually unstable. If the disk is gravitationally unstable, its gas would disappear in a several dynamical times by gravitational torque. The dynamical time is estimated to be of the order of the Keplerian orbital period at the outer radius of the disk r =1500 AU, and it is about 6×10^4 years (much shorter at the inner part) , which is comparable to the age of source A and shorter than the life time of the protostar. Consequently, the disk seems to be unstable through the evolution of protostar phase.

5.2 Origin of compact blue-wing component around source A ; gas heated by interaction with a strong wind inside the disk ?

We will discuss about two possible origins of compact blue-wing emission around source A. One of the possibilities is that it is emitted by the inner part of the Keplerian disk, and another is the emission from the gas accelerated by the interaction with a strong wind inside the disk. In the P-V diagrams, the compact blue-wind components seem to be located at the higher velocity parts of Keplerian rotation (see Figure 5.1), which is very indicative of the former origin. The velocity of the blue wing is kinematically consistent with Keplerian motion at r = 10-30 AU for M_* = 0.2-0.5 $M_\odot$. The brightness temperatures are 6.1 K at V_{LSR} = 0.28 km s^{-1} for $C^{32}S$ $J = 2-1$ and 8.9 K at V_{LSR} = -0.19 km s^{-1} for $C^{32}S$ $J = 3-2$. However, these observed brightness temperatures of the wing component are higher than the dust equilibrium temperature in Keplerian disk of $T = (L_*/4\pi\sigma r^2)^{0.25}$, which is estimated to be 190-330 K, considering the beam dilution effect by a factor of 2(beam area) / πr^2, which is 80-110. In addition there is no corresponding redshifted wing component observed, although the Keplerian disk should have a symmetric kinematical structure of rotation. It is hard to explain the asymmetry by the Keplerian disk origin. Hence it is difficult to interpret that the blueshifted wing emission as originating in the Keplerian rotating gas around source A. On the other hand, the latter origin does not conflict with the asymmetry. The hot core in Ori-KL, which is thought to be produced by the interaction of the disk-like structure of dense gas with the strong wind from IRc-2, has an asymmetric distribution; the hot core is located only at one side of the expanding doughnut (Pauls *et al.* 1932; Migenes *et al.* 1989). Furthermore, the hot core-like gas (but small scale version) would be expected at the inside of the disk around source A, if we consider the fact that the double HII regions and H_2O masers are located inside the disk. Actually, shocked molecular gas was found just at source A by the SO observations of Mundy *et al.* (1992). It is plausible that the compact blue wing is due to the gas shock-produced by the strong wind from a central engine in source A.

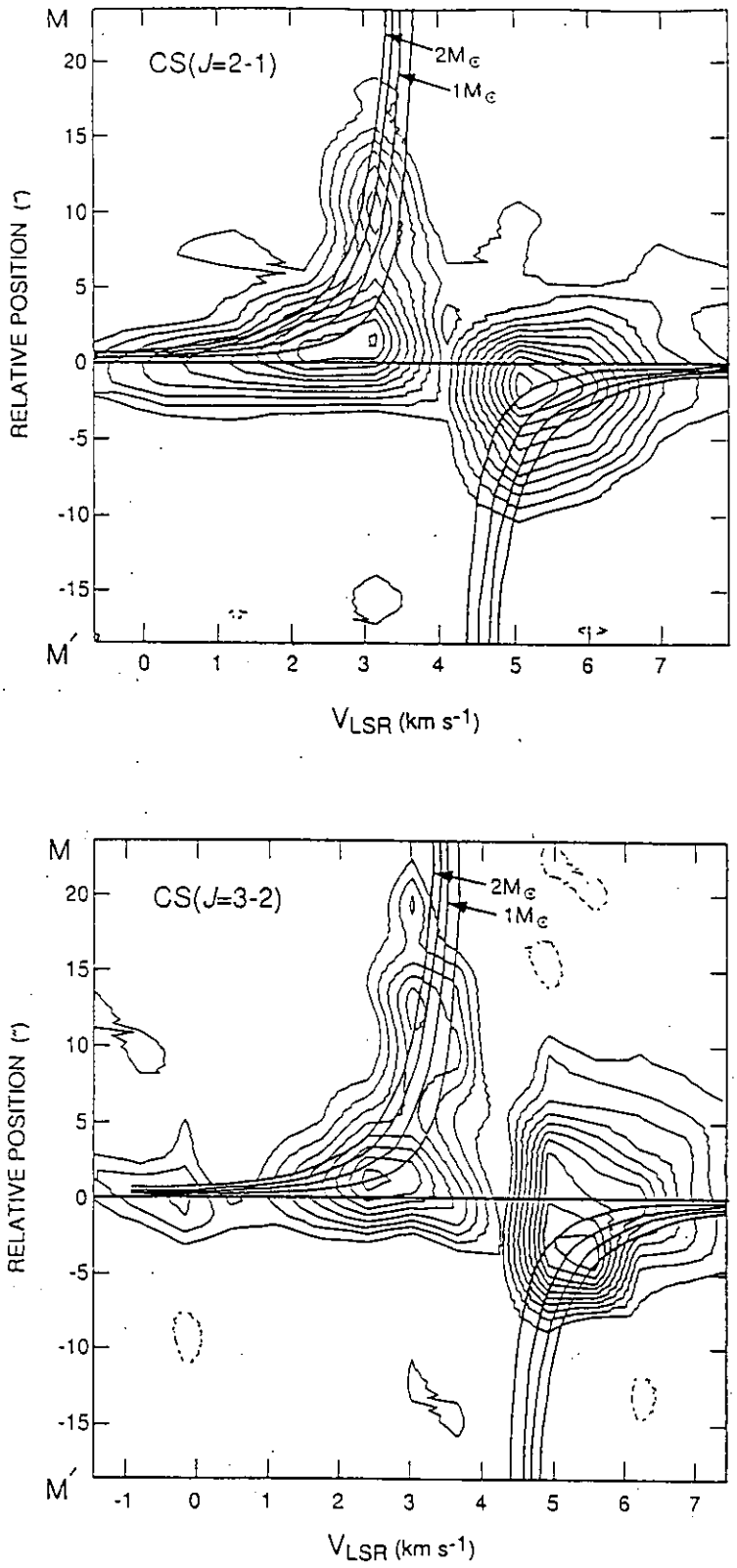

Figure 5.1. Position - velocity maps of (a) the $C^{32}S$ $J = 2 - 1$ and (b) the $C^{32}S$ $J = 3 - 2$ emission along the cut M-M' shown in Fig 3.5. The cutting line is the major axis of the disk-like structure through the position of source A. The contour interval is 1.53 K (1 σ) in the $C^{32}S$ $J = 2 - 1$ map and 1.64 K (1 σ) in the $C^{32}S$ $J = 3 - 2$. The solid line indicates the position of source A. Calculated P-V diagrams of Keplerian rotation gas, centered at 1 and 2 $M_{\odot}$ star at the position of source A, are shown.

6 Structure and evolution of the binary system IRAS 16293-2422

It is very important to know the evolutional stage of the binary system for the investigation of the formation process of binary stars. It is particularly important to know spatial relation between the binary system and the distribution of molecular gas and dust to investigate the formation process of binary systems from dense molecular gas; e.g., relation between source B and the disk structure surrounding source A (Is the orbital plane of the binary in the disk plane ? The disk is common for both sources A and B ?). In this section, we will summarize briefly the difference of gas and dust environments around sources A and B (sec.6.1) , and discuss the evolutional stages of the two stars (sec. 6.2) , age difference of two stars (sec.6.3), and possible configuration of the binary system (sec. 6.4), based on the observational results.

6.1 Spatial structure of the binary system and molecular gas : difference of gas and dust environments around sources A and B

We will again summarize briefly the gas and dust environments for each star to make clear the difference between two stars, and to discuss about the evolutional stage of the two stars in sec. 3.2. Source A has some indications of activities, strong and compact free-free emission, H_2O masers, and the CS "streamer". Both the CS compact wing and the SO compact core (Mundy *et al.* 1992) just located at source A is some indicative of the existence of shocked molecular gas produced by the interaction between strong wind from the central star and the surrounding molecular gas (disk-like envelope) . In addition, a disk-like envelope composed of a large amount of molecular gas ($> 0.3\ M_{\odot}$) is associated with source A and it has rotational motion. It should be noted that the kinematical center of the dense molecular gas traced with $C^{32}S$ as well as $C^{34}S$ is found to be at source A.

On the other hand, there exist no indications of such activities as free-free, H_2O, and shocked molecular gas in source B. Instead, a compact dust disk is associated with source B; a very compact VLA source with a spectral index of about 2 was found for source B and

also a very compact millimeter source was revealed by our 98 and 147 GHz observations with 2″.6 x 1″.7 and 2″.0 x 1″.4 beams, respectively. In addition to the compact disk, a dust envelope is surrounding source B, but only a small amount of molecular gas is found to be closely associated with the source.

In summary, the 2000 AU scale molecular envelope is more massive around source A than source B, while the 500 AU scale dust envelope has almost the same mass. The compact disk around source A is less massive than that around source B. The difference of the gas and dust environments around sources A and B is tabulated in Table 6.1.

6.2 Implications of the spatial structure and the physical nature ; binary composed of a protostar and a young T Tauri star ?

It is very probable that source A is just in an active phase of protostar deeply embedded in the dense gas envelope, because source A has free-free emission, H_2O masers, and shocked molecular gas. On the contrary, source B shows no clear such activities, already has a "massive" compact disk, and has no dense molecular gas envelope like the "massive" disk-like envelope seen around source A.

According to a current theory of star formation (Shu, Adams and Lizano 1987), star formation begins with the collapse of a rotating isothermal sphere forming a protostellar core at the center. On the course of the collapse an accretion disk forms around the protostar as a consequence of conservation of angular momentum. As the matter falls onto the central object, the accretion disk grows until its envelope disappears through accretion into the central protostar or brow-off by the molecular outflow.

This scenario is supported by the recent observations with the NMA. Ohashi *et al.* (1991) found that as an embedded protostar evolves to a T Tauri star, the $C^{32}S J = 2 - 1$ emission becomes invisible while the dust continuum emission becomes visible. They interpreted these results as follows: the extended molecular envelope disperses away or accretes into the center while the compact disk forms and grows through dynamical accretion in the course of the evolution from an embedded protostar to a T Tauri star.

We can speculate from the above discussion that source B might be in elder protostar phase than source A or in young T Tauri phase like HL Tau or DG Tau, if we consider the obtained typical observational properties of mainly single young stellar objects (Ohashi *et al.* 1991).

Around source A a molecular envelope still exists to fall onto a center and the central compact disk have not yet grown. Around source B the envelope begin to disappear, while the accretion disk have grown to possess a large mass.

The T Tauri star would be sufficiently obscured in the IRAS 16293-2422 region containing a large amount of molecular gas. The rough estimation of the age difference between source A and B, based on the above arguments, is presented in the following subsection.

However, it should be mentioned that binary stars, protostars and T Tauri stars in binary systems, show different structures of molecular gas and dust and different evolution from those in single stars; e.g., the lower mass companion might not have a disk-like envelope around it because of the tidal force from the central more massive star (or the star, disk, and envelope system). As well as single stars, binary young stellar objects should be investigated systematically in order to search typical nature of the gas and dust environments and also typical trend of the evolutional change of the environments.

6.3 Rough estimation of age difference between sources A and B

If the age difference is much larger than the age of both molecular outflows, one younger engine is expected to have produced the outflows. We estimate the age difference below.

i) Case 1

Applying the above mentioned scenario of disk formation (or growth) to these sources, we are able to make a coarse estimation of an age difference between sources A and B. If any compact disks grow with the same mass accretion rate on the disk throughout the protostellar phase, the difference between the masses of the disks indicates the age difference of the disks,

and then the age difference of the central stars considering the stars have the same age as the disks. Using the derived masses of the compact disks for sources A and B, and assuming the mass accretion rate onto the disk, $1.3 \times 10^{-6}\ M_{\odot}\mathrm{yr}^{-1}$, the age difference are roughly estimated as

$$\Delta t = \frac{M_{B.disk} - M_{A.disk}}{\dot{M}_{acc.disk}} \approx 2 \times 10^{4}\mathrm{yr}. \quad (7)$$

The assumed mass accretion rate onto disk, $\dot{M}_{acc.disk}$, is derived based on the following arguments. In ρ Ophiuchi molecular cloud the mass infall rate is estimated to be $\sim 1.3 \times 10^{-5}\ M_{\odot}\ \mathrm{yr}^{-1}$ for the assumed gas temperature of 40 K. The mass accretion rate onto disk itself (i.e., mass growth rate of the disk) is thought to be about 10 % or less, if we consider the disk instability (much higher rate will cause the gravitational instability of the disk). It should be noted that the estimated age difference has a large uncertainty (about a factor of 10) introduced by each uncertainty of the masses of the compact disks and $\dot{M}_{acc.disk}$.

ii) Case 2

If we assume that source A is in a protostar phase and source B is in elder protostar phase than source A or in younger T Tauri phase like HL Tau or DG Tau, the age of source A should be several $\times 10^{4}$ and that of source B should be between a few $\times 10^{5}$ and several $\times 10^{5}$ years. Then, the age difference is 10^{5} - several $\times 10^{5}$ years. This is roughly consistent with the difference estimated in case 1. An age difference might be 10^{5}-10^{6} years.

Recently Hartigan *et al.* (1994) carried out the survey of 26 binary T Tauri stars and placed these in an H-R diagram. They claimed that one-third of the binary T Tauri stars showed real age differences, moreover the less massive component was usually younger than the more massive one. The age differences were typically $\leq 10^{6}$ yr. They explained these results by observational evidence that the collapse times for higher mass stars are shorter than those for lower mass stars (Hillenbrand *et al.* 1992). Our interpretations that source B is more massive than source A and hence source B is older than source A is consistent with their results.

6.4 Spatial relation between the binary system and molecular gas : possible configuration of the binary system

It is very important to know spatial relation between the binary system and the molecular gas for the investigation of the formation process of the binary system from dense molecular gas; *e.g.*, relation between source B and the disk structure surrounding source A. Especially, it is very interesting whether the orbital plane of the binary is on or off the disk plane, and whether the disk is common for both sources A and B. In this section, we will discuss about possible configuration of the binary system, and also discuss the spatial relation based on the observational results.

It would be reasonable to identify IRAS 16293-2422 with an apparent separation of 840 AU as a binary system for the following reason. According to the recent report by Larson (1995) on the investigation of the dependence of the average companion surface density on the separation using the accumulated observational data in Taurus region, the average T Tauri stars has a little more than one companion within 0.04 pc, or 8200 AU. This suggests that two stars with separation smaller than 8200 AU forms a bound system with high probability, although Taurus region might not have a typical physical nature of star forming regions.

6.4.1. Assumptions and equation

We can basically estimate a possible configuration of the binary sources A and B, assuming the followings:

(1) sources A and B are gravitationally bound, and

(2) each source (with dust envelope and/or compact disk) rotates in circular orbit around the common center of mass.

By introducing two appropriate angles θ and ψ (see Figure 6.1) specifying the orientation of the binary orbital plane and binary configuration in it, we can derive the following equation (see Appendix in detail).

$$\frac{V_{relative}^2 \, R_{app}}{GM_{tot}} = cos^3\theta \; sin^2\psi, \tag{8}$$

where M_{tot} is total mass of protostars with the dust envelopes and/or the compact disks for both sources A and B, $V_{relative}$ is relative velocity between sources A and B, and R_{app} is the apparent separation of the binary, 840 AU. By substituting these parameters, M_{tot} , $V_{relative}$, and R_{app}, with appropriate values, we can obtain the allowed ranges of the introduced two angles.

The parameters used here, θ and ψ, are related to familiar parameters i and φ, the inclination angle and phase angle measured from the disk major axis, by the following equations (see Figure 6.2) .

$$cos\theta = \sqrt{cos^2\varphi + sin^2\varphi cos^2 i}, \tag{9}$$

$$cos\psi = \sqrt{sin^2\varphi + cos^2\varphi cos^2 i}. \tag{10}$$

Using the equations, we can obtain the ranges of θ and ψ for the case of coplanar binary system with disk plane (on-plane binary case). These are $60° < \theta < 85°$ and $1° < \psi < 4°$, adopting $60° < i < 85°$ and the apparent phase angle of 80°.

6.4.2. Limitation to configurations (angles θ and ψ), and implications

Substituting $V_{relative}$ = 1 km s^{-1} and M_{tot} = 1.24 $M_\odot$ (see Appendix), the configuration of the binary is calculated to be $-28° < \theta < 28°$ and $56° < \psi < 90°$. These ranges of θ and ψ mean that sources A and B are not a coplanar binary system with the disk around source A (see Figure 6.3). The range of the real binary separation is estimated to be 840 AU $< R <$ 950 AU and that of the rotational period P is $2.1 \times 10^4 yr < P < 2.5 \times 10^4 yr$. The binary separation of 840 - 950 AU is wider than an average separation of pre-main-sequence binaries (Mathieu 1994). We can estimate the rotational time scale of the parent molecular core to be $\sim 4 \times 10^4$ yr, based on the $C^{32}S$ observations by Menten *et al.* (1987). The rotational period

of the binary is consistent with that of the parent core.

The estimated ranges of two angles, θ and ψ, implies that the plane of the binary orbit and that of the disk around source A is not coplanar. One possible explanation for forming such a configuration is as follows; (1) A parent cloud core begins collapsing with its rotational axis parallel to magnetic field direction, forming a rotating ring or disk structure. An azimuthal angular momentum of the gas is gradually lost and the gas is accreted. (2) On the course of the collapse two fragments forms in the ring or disk structure with its orbital axis parallel to the rotational axis of the parent cloud core. (3) The angular momentum due to the motion perpendicular to the orbital plane invariant during the accretion. Finally this angular momentum becomes dominant near the center and produces the circumstellar disk, which is not aligned with the orbital plane. Furthermore the circumstellar disk is roughly parallel to the magnetic field direction. One interpretation is that the magnetic field strength is not strong enough to surpass the effect of the initial angular momentum to form the disk.

Table 6.1 Difference of the gas and dust environments around sources A and B

Source A	
strong compact free-free emission (double) [a]	
H_2O masers [a]	
possibly compact dust disk [b]	($0.01 M_\odot$)
500 AU scale dust envelope [b]	($0.3 M_\odot$)
large amount of molecular gas : CS disk [b]	($0.23 M_\odot$)
Interaction with wind (shocked molecular gas)	
SO compact core [c]	
CS compact blue-wing component [b]	($0.01 M_\odot$)
Interaction with outflow	
CS "streamer" [b]	($0.024 M_\odot$)
Source B	
compact dust disk [b]	($0.03 M_\odot$)
500 AU scale dust envelope [b]	($0.5 M_\odot$)
small amount of molecular gas : CS core [b]	($0.05 M_\odot$)

Reference -- a. Wootten 1989; b. this work; c. Mundy et. al. 1992.

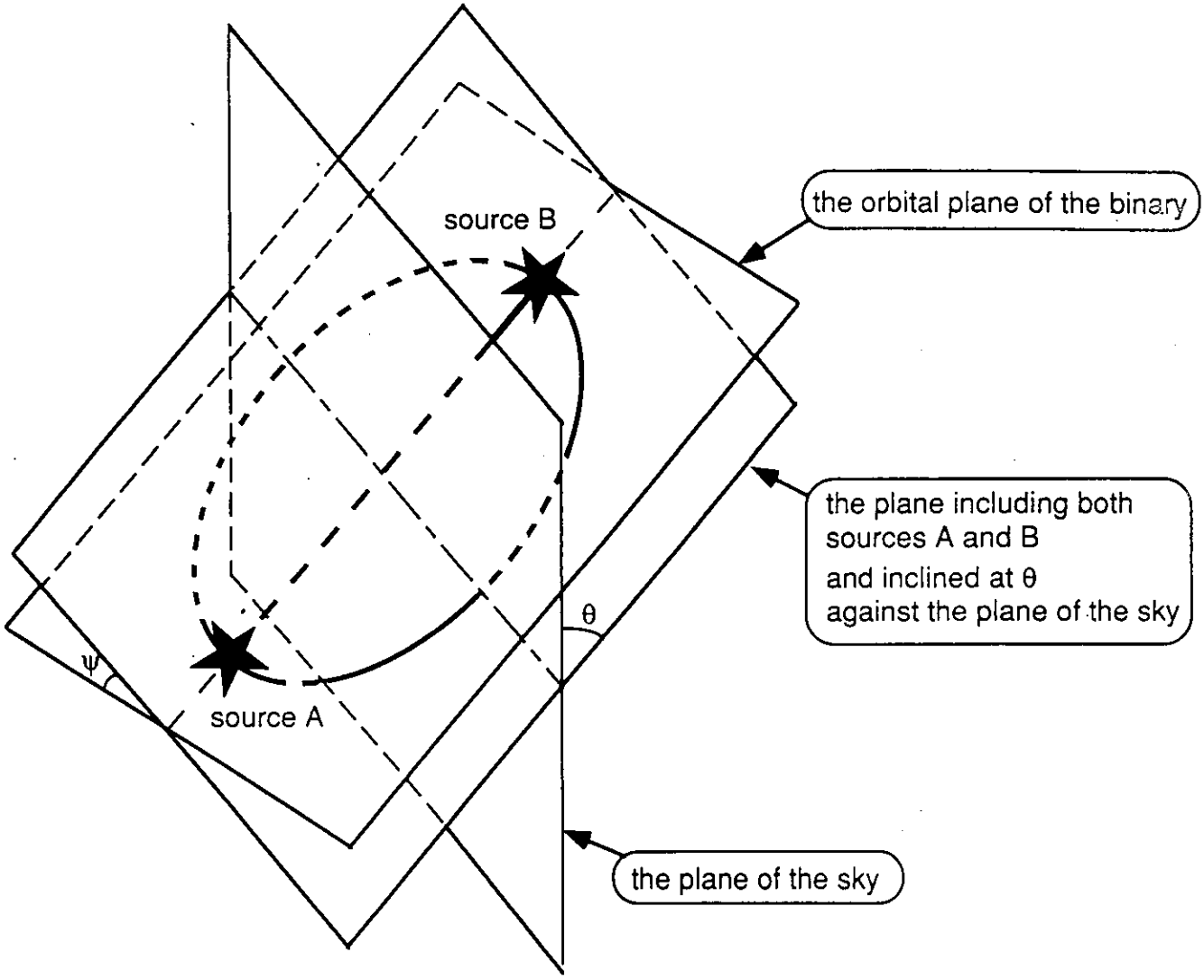

Figure 6.1. Schematic of the binary orbital plane expressed by two angles θ and ψ. θ is an angle between the axis connecting two sources and the plane of the sky and ψ is an angle between the orbital plane of the binary and the plane including both sources and being inclined at θ against the plane of the sky.

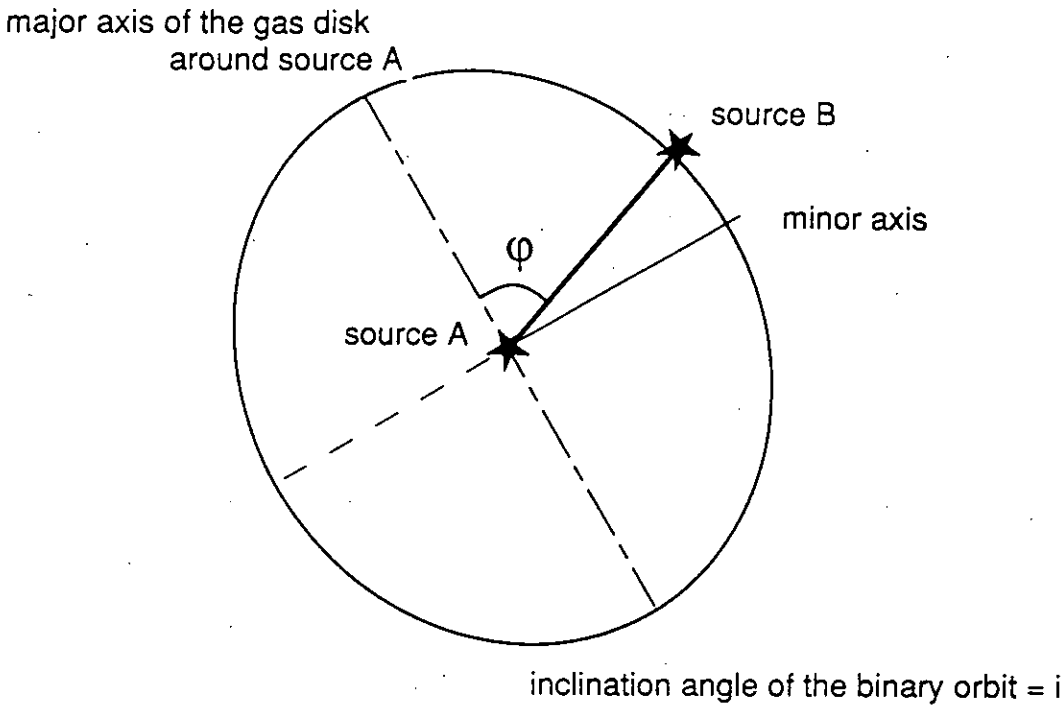

Figure 6.2. Schematic of the binary orbital plane expressed by two angles i and φ. i is an inclination angle of the orbital plane and φ is a phase angle measured from the disk major axis.

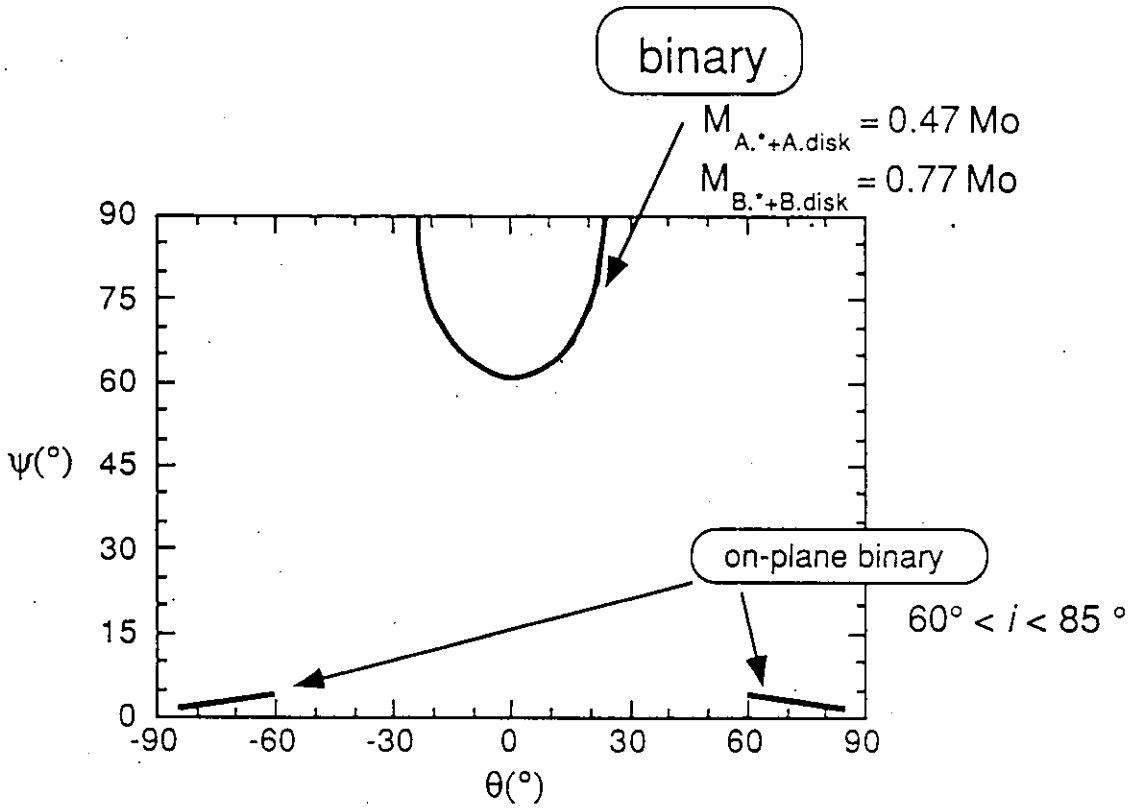

Figure 6.3. Diagram showing the allowed range of θ and ψ for the following two case: (1) a possible binary configuration calculated using the equation (9) for M_{tot} = 1.24 $M_{\odot}$ and $V_{relative}$ = 1 km s^{-1} , and (2) on-plane binary calculated using the equations (10) and (11).

7 Outflow phenomena and the binary system

7.1 Engine(s) of the two pairs of outflows

7.1.1. Source A as an engine of the more prominent outflow

In the previous section, we have summarized the difference of the observational properties between the two sources A and B and it was indicated that only source A shows activities such as compact HII regions, H_2O masers (Wootten 1989), and shocked molecular gas. Considering these activities, source A is suggested to be an engine of the two pairs of bipolar outflows (Rodriguez *et al.* 1989, Terebey *et al.* 1992). On the other hand, it is very likely that source A is at least an engine of the more prominent outflow (with PA=110°), because there exist some evidences showing that source A is associated with that outflow; 1) the direction of the low velocity streamer around source A is just coincident with that of the outflow, and 2) the disk-like structure roughly perpendicular to the outflow seems to be responsible for the formation (or collimation) of the bipolar outflow.

7.1.2. Source A as an engine of the less prominent outflow ?

It is not clear whether source A is also the engine of the less prominent outflow, because no features related to this outflow have been found around source A. Therefore, there exists two possibilities on the engine of the less prominent outflow; one is source A and another is source B. If the estimated age difference is real and if we consider that a typical duration of molecular outflow is about a few $\times$ 10^4 years, it is unlikely that both sources A and B have outflow activities simultaneously; source B is not an engine of the less prominent outflow. In addition. the dynamical time scales of the two pairs of the molecular outflows are estimated to be 4-6 $\times$ 10^3 yr and 0.9-1.4 $\times$ 10^4 yr, respectively (Mizuno *et al.*1990). The difference between the ages of the outflows is much smaller than the age difference of the sources and this fact also suggests that source B is not an engine of the less prominent outflow.

If source A is the engine of the less prominent outflow, the outflow direction was changed within a time scale of about a few $\times$ 10^4 years because the two outflows have different direction and the age of the less prominent outflow is longer by a few $\times$ 10^4 years than the more prominent one. One possible mechanism to explain the change of the outflow direction is a disk precession due to a binary effect. This mechanism and the possibility are discussed in the following sub-section together with the other possible mechanisms.

7.1.3. Possibility of Source B as an engine of the less prominent outflow

In the case that source B is the engine of the less prominent outflow, there are some problems which should be addressed; 1) Why are there no activities of the central star ? 2) Can source B produce the bipolar outflow with no disk-like structure of molecular gas around it ? Walker *et al.* (1994) argued that both sources A and B drive the outflow within the dynamical time scales of the outflow, based on the morphology of the CS outflow images of Walker *et al.* (1990). However, in our maps of $C^{32}S$ $J = 3 - 2$ and $C^{32}S$ $J = 2 - 1$, there is no CS features associated with source B like the $C^{32}S$ low velocity streamer associated with source A.

7.2 Binary effect on outflow; disk precession ?

Several mechanisms have been proposed to explain a phenomenon that a single protostar drives two outflows. First is that the outflow dynamically interact with ambient material and split into two directions (Mizuno *et al.*1990), and second is that the outflow lie on the plane of the sky and appears to consist of two lobes (Cablit and Bertout 1986). Third possibility is the disk precession due to a binary effect (the disk around the driving source precess; Fukue 1986).

We have discovered a rotating disk around source A by the $C^{34}S$ $J = 2 - 1$ observations and the position angle of the rotational axis of the disk has been found to be about 120°. This gas disk, or probably the inner part of it, may collimate the outflow. However the position angle of the direction of the axis connecting the binary sources A and B is about 130°. It

is tempting to interpret that the gas disk precess around the binary axis by the gravitational effect of source B. Thus we try to examine an effect of the disk precession. The precession period of the disk around source A is

$$P = \frac{1.3(M_{A.*} + M_{A.dust})^{0.5} R^3}{(M_{B.*} + M_{B.dust}) r^{1.5} \cos\beta}, \tag{11}$$

where $M_{A.*}$ and $M_{B.*}$ are masses of the central protostars for sources A and B, $M_{A.dust}$ and $M_{B.dust}$ are masses of the dust envelopes and/or compact disks around sources A and B, R is the separation of the binary, r is radius of the disk around source A and β is the angle between the disk equatorial plane and the binary orbital plane (Petterson 1977). By adopting values estimated in the earlier subsections, $M_{A.*} + M_{A.dust}$ = 0.42 $M_{\odot}$, $M_{B.*} + M_{B.dust}$ = 0.79 $M_{\odot}$, r = 1600 AU, β = 80°, and R = 900 AU , the precession period is evaluated to be $\sim 3.1 \times 10^4$ yr.

The precession period of $\sim 3.1 \times 10^4$ yr is a few times larger than the difference between the dynamical time scales of two outflows, which is about 1.1×10^4 yr. Thus the disk precession may explain that two outflows originate from source A if the outflow phenomena are successive and occur a few times during one precession period. In fact recently Bachiller *et al.* (1994) reported that the molecular outflow from L1551 IRS5 is successive, whose timescale is $\sim$ 2-3 $\times 10^4$ yr. If the successive outflow is a common feature of the protostars, it is likely that the outflow from source A is also successive.

Actually, however, it is considered that inner portion of the disk controls the direction of the outflow (Nakano in private communication). Adopting r = 50 AU, the precession period is calculated to be 2.8×10^6 yr which is much longer than the difference between the dynamical time scales of two outflows. Thus we conclude that it is difficult to explain the multiple outflows by the disk precession.

8 Summary

Aperture synthesis observations for IRAS 16293-2422 were carried out using the Nobeyama Millimeter Array (NMA) with the molecular lines of $C^{32}S$ $J = 2 - 1$, $J = 3 - 2$, and $C^{34}S$ $J = 2 - 1$, and with 98 and 147 GHz continuum emissions. The derived features of molecular gas are as follows: (1) Molecular gas disk just centered at source A was found in the $C^{34}S$ $J = 2 - 1$ maps. The velocity structures of the $C^{32}S$ $J = 3 - 2$ and $C^{32}S$ $J = 2 - 1$ maps show that the kinematical center of the molecular gas is also centered at source A and the molecular gas is rotating around source A. These facts suggest that there exists a rotating disk of molecular gas around source A. The mass and the size of the disk are 0.23 $M_{\odot}$ and 3200 AU $\times$ 1300 AU, respectively. The disk has a position angle of 30°, which is roughly perpendicular to the direction of the prominent one of two outflows. (2) EW elongation of molecular gas was found and seems to be associated with source A. The mass is 0.024 $M_{\odot}$. The direction of the elongation is roughly coincident with that of the prominent one of two outflows. It is, therefore, likely that this feature is associated with the prominent outflow. (3) It was found that there exists a compact blue-wing emission centered at source A. The mass is 0.01 $M_{\odot}$. (4) Molecular gas was found to exist closely associated with source B with the velocity width of about 2 km s^{-1} . The mass is 0.05 $M_{\odot}$.

The derived dust environments are as follows: (1) It was revealed from our high-resolution maps at 98 and 147 GHz that there exist very compact cores just associated with both sources A and B. The spectral indices of the cores are estimated to be ~ 2. These observational results, the compact distribution and relatively flatter spectrum, suggest that each compact dust core is a dust disk surrounding each central protostar. The H_2 mass of the compact disk around sources A and B was estimated to be 0.01 $M_{\odot}$ and 0.03 $M_{\odot}$, respectively. (2) An extended dust envelope also exists around each of source A and B. The spectral indices are estimated to be ~ 3.5. The H_2 mass of dust envelopes around sources A and B was estimated to be 0.3 $M_{\odot}$ and 0.6 $M_{\odot}$, respectively.

In summary, the 2000 AU scale molecular envelope is more massive around source A than source B, while the 500 AU scale dust envelope has almost the same mass. The compact disk

around source A is less massive than that around source B. Figure 8.1 shows the schematic image of IRAS 16293-2422 based on our observations.

These observational evidences imply that the two sources are in the different evolutionary phases. Around source A a molecular envelope still exists to fall onto a center and the central compact disk have not yet grown. Around source B the envelope begins to disappear, while the accretion disk have grown to possess a large mass. It is very probable that source A is just in an active phase of protostar deeply embedded in the dense gas envelope, considering that source A has free-free emission, H_2O masers, and shocked molecular gas. Source B might be in elder protostar phase than source A or in young T Tauri phase. An age difference between sources A and B is estimated to be 10^4 - 10^6 years.

The configuration of the binary system is calculated using the quantities obtained by our observations, with relative velocity of sources A and B of 1 km s^{-1} and total mass of central stars with the dust envelope and circumstellar disks of 1.24 $M_\odot$. The estimated configuration implies that the plane of the binary orbit and the disk around source A is not coplanar.

We investigate the kinematics and the dynamical instability of the molecular gas disk around source A. The rotation velocity seems to be roughly consistent with or slightly smaller that the estimated Keplerian velocity. However it is not clear whether the disk is rotationally supported or not, because of large uncertainties in the rotation velocity and the stellar mass. The disk mass of 0.53 $M_\odot$ (the compact dust envelope and the gas disk) is comparable to or higher than the stellar mass of 0.2- 0.5 $M_\odot$. This means that the disk is actually unstable.

Considering the activities associated with source A, source A is suggested to be an engine of the two pairs of bipolar outflows. We have discovered a rotating disk around source A, and rotation axis of the disk is found to be different from the binary axis. It is possible that the gas disk around source A may precess around the binary axis under the gravitational effect of source B. The disk precession could explain that two outflows originate from source A if we consider the radius of the disk of 1600 AU. However, it is considered that inner portion of the disk controls the direction of the outflow. Thus we conclude that it is difficult to explain the multiple outflows by the disk precession.

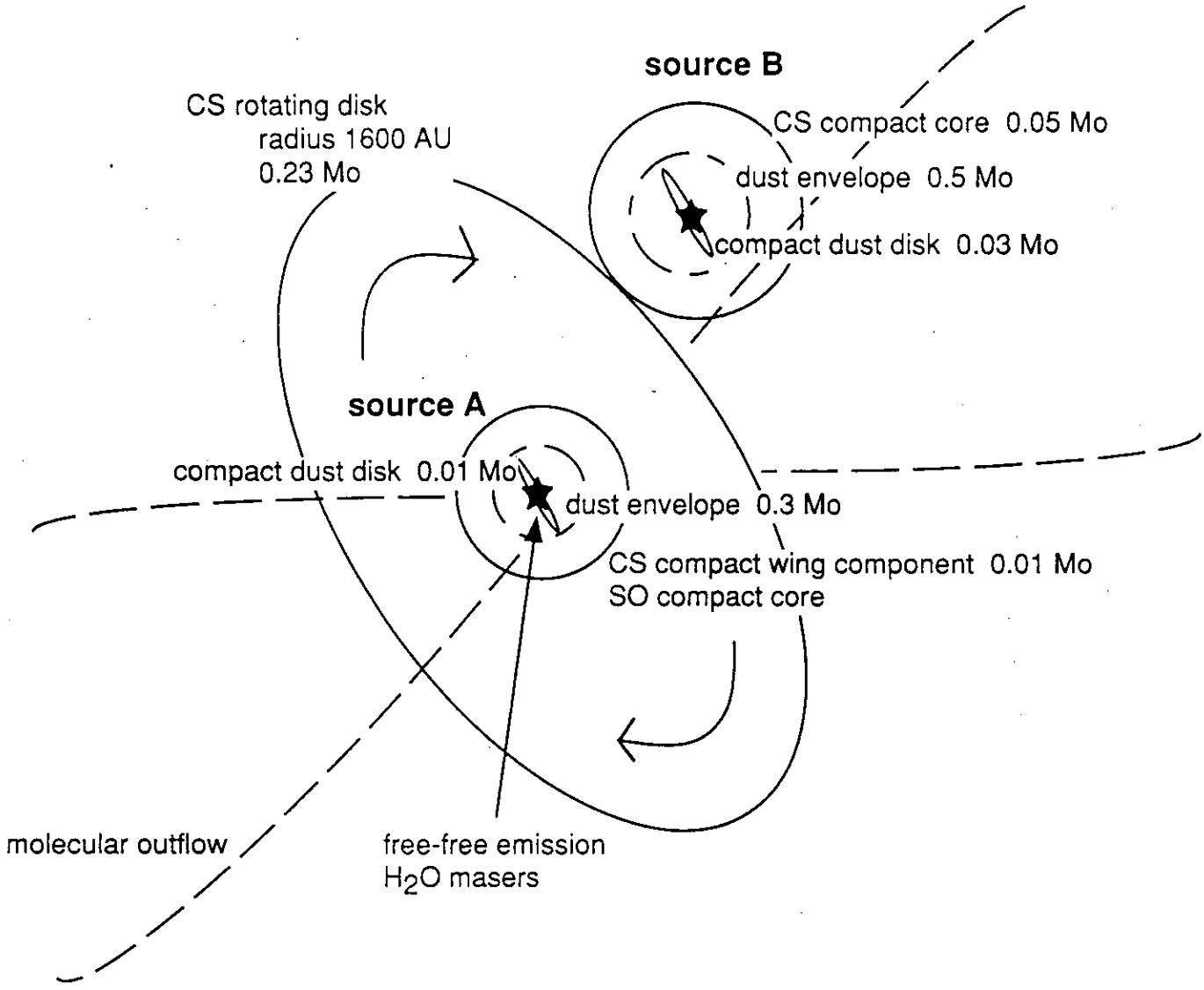

Figure 8.1. Schematic of IRAS 16293-2422 binary system. The $C^{34}S$ disk-like structure around source A shows rotating motions. Source A, with which the free-free emission and a cluster of H_2O masers are associated, drives the molecular outflows. The growth of the dust disk around source B is more advanced than that around source A.

Appendix

Estimation of possible binary configuration

i) Basic Concept

We can basically estimate a possible configuration of the binary sources A and B, assuming the followings:

(1) sources A and B are gravitationally bound, and

(2) each source (with dust envelope and/or compact disk) rotates in circular orbit around the common center of mass.

Actually, if we can know the following quantities:

1) total mass (mass of protostar, M_*, and mass of dust envelope and/or compact disk, M_{dust}) inside the binary orbit, and

2) line-of-sight velocities of gas systems associated with sources A and B,

we can roughly estimate

1) separation of two stars, R, and

2) configuration of the binary orbit specified by two angles introduced below,

by using the following simple equation.

$$R = \frac{G(M_{A.*} + M_{A.dust}) + (M_{B.*} + M_{B.dust})}{V_{rot}^2}, \tag{A1}$$

where R is real binary separation, $M_{A.*}$ and $M_{B.*}$ are masses of central protostars for sources A and B, $M_{A.dust}$ and $M_{B.dust}$ are masses of the dust envelopes and/or the circumstellar disks around sources A and B, and V_{rot} is rotational velocity of the binary.

Introducing θ and ψ, where θ is an angle between the axis connecting two sources and the plane of the sky and ψ is an angle between the orbital plane of the binary and the plane including both sources and being inclined at θ against the plane of the sky (see Figure 6.1 for θ and ψ) , the real separation is

$$R = \frac{R_{app}}{cos\theta} \text{ (AU)}, \tag{A2}$$

where R_{app} is the apparent separation of the binary, 840 AU.

The rotational velocity of each binary star, V_{rot}, is related to the relative line-of-sight velocity for two stars, $V_{relative}$, as

$$V_{rot} = \frac{V_{relative}}{cos\theta\ sin\psi} \text{ (km s}^{-1}\text{)}. \tag{A3}$$

Using the above three equations, we can derive the following equation.

$$\frac{V_{relative}^2\ R_{app}}{GM_{tot}} = cos^3\theta\ sin^2\psi. \tag{A4}$$

ii) estimation of $V_{relative}$ and total system mass

The systemic velocities of sources A and B are estimated from appearance of the CS emissions associated with each source in the $C^{32}S$ $J = 2 - 1$ and $J = 3 - 2$ channel maps (Figures. 3.1 and 2.2). Since the CS emissions associated with source A appear over the velocity range from V_{LSR} = 0 km s^{-1} to 8 km s^{-1}, the systemic velocity of the CS emissions associated with source A may be V_{LSR} = 4 km s^{-1}, which is the same as that of the parent molecular cloud. While the CS emissions associated with source B appear from V_{LSR} = 2 km s^{-1} to 4 km s^{-1}, and the systemic velocity of the CS emission associated with source B may be V_{LSR} = 3 km s^{-1}, which is blueshifted by 1 km s^{-1} relative to that associated with source A. Here we assume that the systemic velocities of the central protostars are the same as those of the CS emissions associated with each source, 4 km s^{-1} and 3 km s^{-1} for source A and source B, respectively. Thus the relative velocity of two sources is about 1 km s^{-1}.

From the dust continuum emission we can evaluate the masses of the dust envelopes and the circumstellar disks to be 0.30 $M_\odot$ and 0.49 $M_\odot$ for source A and source B, respectively, assuming the dust temperature of 40 K and the β index of 1.5 and 0 for the dust envelope and the circumstellar disk, respectively.

Next we deduce the masses of the protostars. We assume that the whole bolometric luminosity of 27 $L_{\odot}$ is due to accretion. The accretion luminosity is expressed as

$$L_{acc} = \frac{GM_{*}\dot{M}}{R_{*}} \tag{A5}$$

where $\dot{M}$ is mass accretion rate onto the star, which is $\sim 1.3 \times 10^{-5}\ M_{\odot}\mathrm{yr}^{-1}$ in the case of the gas temperature of 40 K, and R_{*} is the radius of the protostar, which is 4 $R_{\odot}$(Adams and Shu 1985). Substituting these values into above equation, we derive the mass of protostars $M_{A.*} + M_{B.*}$ to be $\sim$ 0.45 $M_{\odot}$. Assuming that the mass ratio M_{*}/M_{disk} is the same for sources A and B, the mass of each protostar is deduced to be 0.17 $M_{\odot}$ and 0. 28 $M_{\odot}$ for source A and source B, respectively. Thus total masses are estimated to be $M_{A.*} + M_{A.dust}$ = 0.47 $M_{\odot}$ and $M_{B.*} + M_{B.dust}$ = 0.77 $M_{\odot}$.

The derived stellar masses are very consistent with those of the compact dust disks, 0.01 $M_{\odot}$ and 0.03 $M_{\odot}$ for sources A and B, respectively, because the disk stability criterion $M_{disk} = 3/4\pi(M_{disk} + M_{*})$ (Shu *et al.* 1990) which corresponds to Q = 1, where Q is the stability parameter of Toomre (1964), is roughly satisfied.

REFERENCES

Abt, H. A. 1983, *Annu, Rev. Astron. Astrophys*, **21**, 343.

Adams, F. C. 1990, *ApJ*, **363**, 578.

Adams, F. C. and Shu, F. H. 1985, *ApJ.*, **296**, 655.

Adams, F. C. and Shu, F. H. 1986, *ApJ.*, **308**, 836.

Adams, F. C., Lada, C. J. and Shu, F. H. 1987, *ApJ.*, **321**, 788.

Adams, F. C., Ruden, S. P., and Shu, F. H. 1989, *ApJ*, **347**, 959.

Andre, P., Ward-Thompson, D., and Barsony, M. 1993, *ApJ*, **406**, 122.

Andre, P. 1994, in *Proceedings of the XIIIth Rencontres de Moriond, "The Cold Universe"*, eds. T. Montmerle, C. J. Lada, F, Mirabel, and J. Tran Thanh Van (Editions Frontieres), p179.

Anglada, G., Estalella, R., Rodriguez, L. F., Torrelles, J. M., Lopez, R., and Canto, J. 1991, *ApJ*, **376**, 615.

Bachiller, R., Tafalla, M., and Cernicharo, J. 1994, *ApJ*, **425**, L93.

Barsony, M. and Najita, J. 1990, in *Dusty Objects in the Universe*, ed. E. Bussoletti and A. A. Vittone (Dordrecht: Kluwer), p181.

Batten, A. H. 1973, *Binary and Multiple Systems of Stars*, London:Pergamon.

Beckwith, S. V. and Sargent, A. I. 1991, *ApJ*, **381**, 250.

Beichman, C. A., Myers, P. C., Emerson, J. P., Harris, S., and Mathieu, R. D., 1986, *ApJ*, **307**, 337.

Blake, G. A., van Dishoeck, E. F., Jansen, D. J., Groesbeck, T. D., and Mundy, L. G. 1994, *ApJ*, **428**, 680.

Boss, A. P. 1993, *ApJ*, **410**, 157.

Chapman, S., Pongracic, H., Disney, M., Nelson, A., Turner, J., and Whitworth, A. 1992, *Nature*, **359**, 207.

Chikada, Y., *et al.*. 1987, Proc. IEEE, **75(9)**, 1203.

Clarke, C. J., and Pringle, J. E. 1991, *MNRAS*, **249**, 584.

Dickman, R. L. 1978, *ApJS*, **37**, 407.

Duquennoy, A. and Mayor, M. 1991, *A&A*, **248**, 485.

Emerson, J. P. 1988, in Formation and Evolution of Low-Mass Stars, eds. A.K.Dupree and M.T.V.T. Lago (Dordrecht: Kluwer), 21.

Esatlella, R., Anglada, G., Rodriguez, L. F., and Garay, G. 1991, *ApJ*, **371**, 626.

Fink, R. W. 1981, in *Handbook of Spectroscopy*, Vol. 3, ed. J. W. Robinson (Boca Rotan, Fl.:CRC Press).

Freaking, M. A., Wilson, R. W., Linke, R. A., and Wannier, P. G. 1980, *ApJ*, **240**, 65.

Fukui, Y., Iwata, T., Mizuno, A., Bally, J., and Lane, A. P. 1993, *Protostars and Planets*, eds. Levy, E. H. and Lunine, J. I., (Yucson:Univ. Ariz. Press), p603.

Fuller, G. A., and Myers, P. C., 1987, in *NATO/ASI Physical Processes in Interstellar Clouds*, ed. M. Scholer. (Dordrecht: Reidel).

Ghez, A. M., Neugebauer, G., and Matthews, K. 1993, *AJ*, **106**, 2005.

Hartigan, P., Strom, K. M., and Strom, S. E. 1994, *ApJ*, **427**, 961.

Hillenbrand, L. A., Strom, S. E., Vrba, F. J., and Keene, J. 1992, *ApJ*, **397**, 613.

Jensen, E. L. N., Mathieu, R. D. and Fuller, G. A. 1994, *ApJ*, **429**, L29.

Keene, J. and Masson, C. R. 1990, *ApJ.*, **355**, 635.

Lada, C. J. and Wilking, B. J. 1984, *ApJ*, **287**, 10.

Lada, C. J. 1991, in *The Physics of Star Formation and Early Stellar Evolution*, eds. C. J. Lada and N. D. Kylafis, (Dordrecht:Reidel), p329.

Lada, C. J. 1987 in *I.A.U. Symposium No. 115: Star Forming Regions*, eds. M. Peimbert and J. Jugaku, (Dordrecht: Reidel), p 1.

Larson, R. B. 1995, *MNRAS.*, **272**, 213.

Leinert, Ch., Weitzel, N., Zinnecker, H., Christou, J., and Ridgeway, S. 1993, *A&A*, **278**, 129.

Larson, R. B. 1990, *MNRAS.*, **243**, 588.

Lin, D. N. C. and Pringle, J. E. 1990, *ApJ*, **358**, 515.

Mathieu, R. D. 1994, *Annu. Rev. Astron. Astrophys.*, **32**, 465.

Mathieu, R. D., Walter, F. M., and Myers, P. C. 1989, *AJ*, **98**, 987.

Menten, K. M., Serabyn, E., Güsten, R., and Wilson, T. L., 1987, *A&A.* **177**, L57.

Mezger, P. G., Sievers, A., Zylka, R., Haslam, C.G.T., Kreysa, E., and Lemke, R. 1992, *A&A.* **265**, 743.

Migenes, V., Johnston, K. J., Pauls, T. A., and Wilson, T. L. 1989, *ApJ*, **347**, 294.

Mikami, H. 1995 in private communication.

Mizuno, A., Fukui, Y., Iwata, T., and Nozawa, S. 1990, *ApJ*, **356**, 184.

Mundt, R., Walter, F. M., Feigelson, E. D., Finkenzeller, U., Herbig, G. H., and Odell, A. P. 1983, *ApJ*, **269**, 229.

Mundy, L. G., Wootten, A., Wilking, B. A., Blake, G. A., and Sargent, A. I. 1992, *ApJ.*, **385**, 306.

Mundy, L. G., Wootten, A., and Wilking, B. A. 1990, *ApJ.*, **352**, 159.

Mundy, L. G., Wilking, B. A., and Myers, S. T. 1986, *ApJ*, **311**, L75.

Myers, P. C., 1986, in *Star-Forming Regions*, ed. M. Peimbert, J. Jugaku, (Dordrecht: Reidel).

Myers, P. C., Linke, R. A., and Benson, P. J., 1983, *ApJ*, **264**, 517.

Myers, P. C., and Benson, P. J., 1983, *ApJ*, **266**, 309.

Pauls, T. A., Wilson, T. L., Bieging, J. H., and Martin, R. N. 1983, *A&A*, **124**, 23.

Richichi, A., Leinert, Ch., Jameson, R., and Zinnecker, H. 1995, *A&A*in press.

Rodriguez, L. F., Myers, P. C., Cruz-Gonzalez, I., and Terebey, S. 1989, *ApJ*, **347**, 461.

Rodriguez, L. F., Canto, J., and Torrelles, J. M. 1986, *ApJ*, **301**, L25.

Sandel, G., Aspin, C., Duncan, W. D., Russell, A. P. G, and Robson, E. I. 1991, *ApJ*, **376**, L17.

Sargent, A. I. 1977, *ApJ*, **218**, 736.

Sasselov, D. D., and Rucinski, S. M. 1990, *ApJ*, **351**, 578.

Schloerb, F. P., Friberg, P., Hjalmarson, A., Hoglund, B., and Irvine, W. M. 1983, *ApJ*, **264**, 161.

Shu, F. H.1992, in Protostars and Planets III, eds. E. H. Levy and J. I. Lunine (Tucson: Univ. of Arizona Press), p3.

Shu, F. H.1977, *ApJ*, **214**, 488.

Shu, F. H., Adams, F. C., and Lizano, S. 1987, *Annu. Rev. Astron. Astrophys.*, **25**, 23., **358**, 495.

Shu, F. H., Tremaine, S., Adams, F. C., and Ruden, S. P. 1990, *ApJ*, **358**, 495.

Simon, M., Chen, W. P., Howell, R. R., Benson, J. A., and Slowik, D. 1992, *ApJ*, **384**, 212.

Solomon, P. M., Sanders, D. B., and Scoville, N. Z. 1979, in *The Large Scale Characteristics of Galaxies, IAU Symp. No. 84*, ed. W. B. Burton, (Dordrecht: Reidel), p35.

Sunada, K., Kawabe, R., and Inatani, J. 1993. Int. J. Infrared and Millimeter wave, **14**, 1251.

Tamura, M., Hayashi, S. S., Yamashita, T., Duncan, W. D., and Hough, J. H. 1993, *ApJ*, **404**, L21.

Terebey, S., Shu, F. H., and Cassen, P. 1984, *ApJ*, **286**, 529.

Terebey, S., Vogel, S. N., and Myers, P. C. 1992, *ApJ*, **390**, 181.

Toomre, A. 1964, *ApJ*, **139**, 1217.

van Dishoeck, E. F., Blake, G. A., Draine, B. T., and Lunine, J. I. 1992, in Protostars and Planets III, eds. E. H. Levy and J. I. Lunine (Tucson: Univ. of Arizona Press), p163.

Walker, C. K., Carlstrom, J. E., and Bieging, J. 1993, *ApJ.*, **402**, 655.

Walker, C. K., Carlstrom, J. E., Bieging, J. H., Lada, C. J., and Young, E. T. 1990, *ApJ.*, **364**, 173.

Walker, C. K., Adams, F. C., and Lada, C. J. 1990, *ApJ.*, **349**, 515.

Walker, C. K., Lada, C. J., Young, E. T., Malnoey, P. R., and Wilking, B. A. 1986, *ApJ*, **309**, L47.

Whittet, D. C. B. 1974 *MNRAS.*, **196**, 469.

Wilson, R. W., Jefferts, K. B., and Penzias, A. A. 1970, *ApJ*, **161**, L43.

Wootten, A. 1989, *ApJ*, **337**, 858.

Zhou, S. 1995, *ApJ*, **442**, 685.